Thesis for the degree
Master of Science

Submitted to the Scientific Council of the
Weizmann Institute of Science
Rehovot, Israel

עבודת גמר (תזה) לתואר
מוסמך למדעים

מוגשת למועצה המדעית של
מכון ויצמן למדע
רחובות, ישראל

By
Eran Erdal

מאת
ערן ארדל

מכפל מבוסס נקבים שקוע בנוזל – קונספט חדשני
עבור גלאי תא היטל בזמן בפאזה הנוזלית של גז אציל

Liquid Hole Multipliers – A new concept for large volume noble liquid time projection chamber

Advisor:
Prof. Amos Breskin

מנחה:
פרופ' עמוס ברסקין

February, 2015

אדר תשע"ה

Abstract

Direct dark matter detection is one of the most challenging fields in current experimental physics. Successful detection of dark matter particles will constitute a major step into the realm of physics beyond the standard model. Currently running experiments, dedicated to the search of Weakly Interacting Massive Particles (WIMPs) suggested by a variety of theoretical models, have already ruled out some models and set limits on others. The most sensitive among these experiments employ noble liquid targets (liquid xenon or liquid argon) as the detection medium and are operated in a dual-phase Time Projection Chamber (TPC) configuration. Since the sensitivity of these detectors scales as the mass of their noble-liquid target, increasingly larger detectors are being designed and deployed. However, to reach their ultimate sensitivity future noble-liquid detectors must grow to the multi-ton scale. The use of current detection concepts, may pose significant technological and economical challenges – calling for new developments.

This study focuses on further investigations of the innovative concept of *Liquid Hole Multipliers* (LHMs) as a potential solution for scaling noble-liquid detectors to the multi-ton regime. The idea consists of cascaded multiple UV-sensitive CsI-coated THGEM hole-electrodes, immersed in the noble liquid, and to multiply WIMP-induced photons and electrons via successive electroluminescence processes occurring within the THGEM holes. Previous studies conducted in our group have shown electroluminescence in the holes of a *Thick Gaseous Electron Multiplier* (THGEM) electrode immersed in liquid xenon - occurring at surprisingly low electric fields. In this work, we present our new understanding of the operation mechanism; we show that the electroluminescence occurs within xenon bubbles trapped below the electrode rather than in the liquid phase itself. We present a detailed study of the electroluminescence yield and achievable energy resolution of this new *bubble-assisted LHM* concept as a function of various parameters. We further discuss the identification of a "*super-stable*" state (corresponding to specific thermodynamic conditions) showing an exceptionally good energy resolution with alpha particles stopped in the liquid xenon. In addition, we also describe the design and commissioning of a new liquid xenon cryostat, dedicated to further systematic studies of the LHM concept and its bubble-assisted mechanism; results of its first operation period are presented. The potential application of the LHM to dark matter detection is discussed.

Acknowledgements

It is my pleasure to thank all those who assisted me during my M.Sc. thesis research period at the Weizmann Institute of Science.

First and foremost, I would like to extend special thanks to my supervisor **Prof. Amos Breskin** who granted me an opportunity to take active part in the cutting edge research of particle detection techniques, by guiding my project using his vast knowledge and experience.

Very special thanks to **Dr. Lior Arazi** for his co-guidance and assistance and for countless hours spent together in the laboratory and in meaningful conversations.

Cordial thanks to **Dr. Michael Rappaport** for sharing with me the intimate secrets of vacuum, cryogenics and laboratory hardware, without which my project could have never been as successful.

To **Dr. David Vartsky** for introducing me to the richness of the world of nuclear physics.

To **Dr. Vitaly Chepel** for a most enriching period of working in the lab together.

To My lab colleagues and mates **Dr. Sana Shilstein**, **Dr. Sergei Shchemelinin**, **Artur Coimbra, Itamar Israelashvili** and **Luca Moleri** for useful conversations and support whenever and wherever needed.

To **Oz Diner** and **Benjamin Pasmantirer** for their elegant design of my setup and to **Shlomo Assayag**, **the workshop team** and **Yoel Chalaf** for their devotion to the cryostat construction.

To the **Soreq NRC Radiation Protection Department** group for preparing the Am-241 alpha source used in the MiniX cryostat.

To **Yigal Shachar** and to his team of the physical services for their helping hands.

To **Doron Bar** for his knowledge and assistance in the laboratory's computation and automation.

And last but not least to the administrative team: **Michal Hirshberg**, **Hemda Atziz**, **Natalia Leybovich, Revital Ackler**, **Hadar Alper**, **Yuri Yegudaev**, **Hadar Lappin** and **Hila Shtudiner** for their proficient and efficient support.

Contents

1 Introduction 4
1.1 Direct dark matter detection 4
1.2 Noble liquid dual phase TPC detectors 5
1.3 Background suppression 5
1.4 Scaling up noble-liquid TPCs 6
1.5 Liquid Hole Multipliers (LHM) 7
1.6 First experiments for electroluminescence in THGEM holes 9
2 Experimental setups 12
2.1 The large liquid xenon R&D facility – WILiX 12
2.2 New liquid xenon R&D facility – MiniX 14
2.2.1 Motivation and desired specifications 14
2.2.2 Cryogenics and thermodynamics control 16
2.2.3 The detector assembly 18
2.2.4 G-MiniX – looking into the xenon 19
3 Results in WILiX 21
3.1 Bubbles hypothesis validation 21
3.2 Study of S2 properties 23
3.3 “Super-stable” conditions 29
3.4 S1 variation with THGEM voltage 31
3.5 Estimates of vapor layer thickness 32
4 Results in MiniX 34
4.1 First liquefaction 34
4.2 Generation of bubbles on thin resistive wires 35
4.3 LHM element with resistive wires for bubbles creation 37
4.4 Charge collection 39
5 Discussion and future plans 42
6 Bibliography 45

1. Introduction

1.1 Direct dark matter detection

Astronomical and cosmological observations over the last decades have found strong evidence that the vast majority of mass-energy content of the universe is not composed of ordinary standard model baryonic matter but consists mainly of dark energy (68%) and Dark Matter (DM, 28%) [1]. DM is hypothesized to be a yet undetected, non-luminous, non-strongly interacting form of matter; it is believed to be responsible, through its gravitational interaction with ordinary matter, for the observed large-scale astronomical structures and motion of stars and galaxies, which are in strong disagreement with expectations based on ordinary matter alone. Many models for DM exists, the most prominent being those of Weakly Interacting Massive Particles (WIMPs); these suggest the existence of non-standard model particles that interact both via gravitation and via the weak (or weak-scale) interaction with baryonic matter [2] [3].

Direct detection of WIMPs, namely the detection of its interaction with ordinary baryonic matter, offers a great challenge in modern experimental physics. A successful detection of WIMPs would be the strongest indication for the existence of particle physics beyond the standard model. The predicted WIMP masses are model-dependent and so are the cross-sections for WIMP interaction with baryonic matter [4]. The latter are very small; e.g. XENON100, with the participation of WIS scientists, set an upper limit of $2 \times 10^{-45}\ cm^2$ for spin-independent elastic WIMP-nucleon scattering [5] at a WIMP mass of $55\ GeV/c^2$; the LUX experiment set an upper limit of $7.6 \times 10^{-46}\ cm^2$ at a WIMP mass of $33\ GeV/c^2$ for the same cross section [6]). The low detection probabilities require DM detectors to have ever larger masses, higher instrumental sensitivity and the lowest-possible background. Direct detection of DM is based on the detection of low-energy WIMP-induced nuclear recoils in a proper target-medium, as reviewed in [7]. These can be detected via three main channels: mechanical energy (i.e. phonons in solid state detectors as in CDMS experiment [8]), scintillation and ionization. While solid state detectors suggest an ultra-high purity and low background experiment comparable to that of liquid noble gases, their up scaling is currently technologically challenging [9]. One of the most advanced methods of direct detection of WIMPs, is the observation of nuclear-recoils

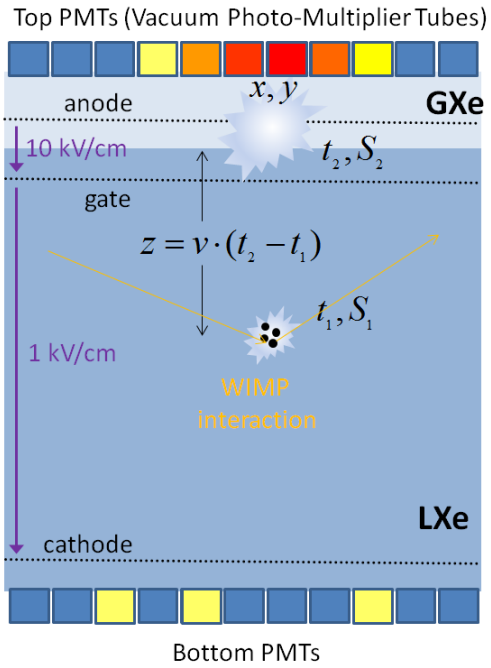

Figure 1 A dual-phase xenon time projection chamber. A nuclear recoil induced by a WIMP interacting in the TPC volume induces scintillation and ionization in the volume. Scintillation light (S1) is recorded with top and bottom arrays of photomultipliers. Ionization electrons are drifting upwards; they are extracted into the gas phase under a strong electric field where they induce electroluminescence (S2). Hit patterns of S2 on the top array allow for the reconstruction of the XY interaction's coordinates position; the time difference between light and charge signals allows for reconstruction of the interaction depth. The S1 and S2 pulse heights are recorded for reconstruction of deposited energy and for background discrimination.

in rare elastic-scattering events off Ar or Xe atoms in a noble-liquid Time Projection Chamber (TPC) detector [10] [11].

1.2 Noble liquid dual phase TPC detectors

Noble liquid TPC detectors, of a dual-phase type (Figure 1), rely on the detection of radiation-induced primary-scintillation photons (emitted in the liquid phase) and ionization electrons (extracted into the saturated vapor phase above the liquid). Currently running experiments are XENON100 [12], Panda-X1 [13] and LUX [14] with liquid xenon (LXe) and DarkSide50 [15] with liquid argon (LAr); in assembly are XENON1T [16] and ArDM [17].

DM noble-liquid TPC detectors are located within large cryostat vessels, with additional complex gas handling and purification systems as well as other infrastructures and control systems. The noble liquid in the dual-phase TPC shown in Figure 1, is in thermodynamic equilibrium with its vapor phase above it. An elastic scattering of a WIMP off a nucleus (here Xe) induces a nuclear recoil, which deposits its energy along a short (nm scale) trajectory by means of ionization and excitation of the surrounding atoms. There are several means by which the de-excitation can occur; of main interest is the formation of an R_2^* excimer (where R stands for a noble gas atom) [10] either at triplet or at singlet state, which, upon decay, emits a scintillation photon to which the medium is transparent. LXe and LAr respective UV emission wavelengths are 178 and 130 nm [10]. In present experiments, the scintillation light is recorded on two arrays of single-photon sensitive vacuum Photomultiplier Tubes (PMT), one at the top and one at the bottom of the vessel (Figure 1). A drift field (usually 0.2-1 kV/cm) is applied between a cathode mesh grid at the bottom of the liquid and a gate mesh placed beneath the liquid level; an anode mesh is placed a few mm above the liquid surface. Electrons drifting upwards (with typical velocity of $\sim 2mm/\mu s$ at the quoted fields [10]) are extracted to the gas phase under a larger electric field (typically $\sim 10\ kV/cm$); they induce electroluminescence in the gas phase - recorded on the top sensors array. The hit pattern on the top array allows for the XY position reconstruction of the event and the time difference between the prompt scintillation (S1) at the site of interaction and the electroluminescence in the gas phase (S2) allows the reconstruction of the Z coordinate, thus allowing a full localization of the event in the detector. S1 and S2 pulse heights (or integrated pulse areas) provide the energy deposited in the detector and their ratio serves for background suppression as discussed below.

1.3 Background suppression

A crucial problem in these rare-event experiments is the efficient suppression of cosmic, environmental, structural and intrinsic background. Cosmic background is dramatically reduced by running DM experiments in deep underground laboratories, with additional active shielding to discard residual muon-induced events. For example, in the forthcoming XENON1T the cryostat is immersed in a large water-Cherenkov tank, used as muon-veto detector [16]. The detector elements, cryostat, shielding and other surrounding parts are constructed of screened radio-pure materials, to keep natural radioactivity background at the lowest possible level.

LXe and LAr are used for self-shielding of residual environmental radiation emitted from the TPC drift-cage, vessel and PMTs. Therefore, an internal part of the noble-liquid volume is

fiducialized. Events occurring outside the fiducial volume are considered background and therefore discarded, hence the importance of localization of the event.

Background inside the fiducial volume results from several sources: energetic gamma photons which scatter once in the sensitive target, leading to recoiling Compton electrons; low-energy beta emissions of residual dissolved impurities (e.g., ^{222}Rn and ^{220}Rn progeny or ^{85}Kr); and lastly – single scatter nuclear recoil events induced by neutrons, which may either result from alpha-n events from the detector components or from residual muon-induced showers not identified by the experiment's muon-veto system. The light and charge yields from the recoil track differ vastly between nuclear and electron recoils. For a given kinetic energy, a nuclear recoil produces less light and much less free ionization electrons compared to a recoiling electron. This phenomenon is a key element in discriminating gamma- and beta-induced background events, by the different ratio of the charge-to-light signals (S2/S1) in LXe-based detectors in LXe based detectors [12]. In LAr, unlike LXe, the decay times of the triplet and singlet states of the excimer differ significantly ($7ns$ vs. $1600\ ns$ in LAr compared to $4ns$ vs. $22\ ns$ in LXe [18]). At denser energy deposition, namely at a nuclear recoil, the ratio of the singlet state to the triplet state will be enhanced. Nuclear recoil and electron recoil can then be discriminated based on pulse shape, assuming fast enough light sensors in LAr. Neutron background, inducing nuclear recoils similar to that of WIMPs, cannot be suppressed in this way. Since LXe and LAr are rather dense targets, and since a WIMP interacts rarely enough to consider a double scatter in the detector impossible, neutrons can be identified when a multiple vertex scatter event occurs [11].

1.4 Scaling up of Noble-Liquid TPCs

The extremely low cross section values for the interaction of WIMPs with baryonic matter leading to an expected event rate of detected events below $\sim 10^{-4}\ events/day/kg\ Xe$ [4] push the detectors to grow larger in volume. The scaling up of the currently running XENON100 detector - from 34 kg of fiducial LXe volume to the forthcoming XENON1T ton detector (~1 ton fiducial volume) and to future multi-ton detectors (e.g. that discussed by the DARWIN consortium for future detectors, including WIS scientists [19]), poses serious concerns about design, operation properties and cost - with current available technologies. Assuming a large target of noble-liquid of the type shown in Figure 1, a prime concern would be maintaining a good S2 signal resolution over the large cross section ($\sim 2m$ diameter) of the TPC. The scintillation in the vapor phase is proportional to the electric field and the distance the electrons travel in the gas phase; therefore, a slight tilt of the liquid surface, level variations, sloshing waves, non-uniformities across the mesh grids - would affect the S2 resolution, thus leading to the loss of discrimination power between a nuclear- and electron-recoils.

This could be potentially overcome by conceiving *single-phase liquid-only detectors*, with good-quality S1 and S2 signals, with accompanying efficient background discrimination. Moreover, the very high cost of UV-sensitive photomultiplier tubes (designed for cryogenic operation), their poor pixilation (few inch PMT diameter) and their limited effective area coverage (filling factor, currently ~50%), as well as radio-impurity issues - call for new photo-sensor solutions. Among current trends in this field are arrays of Geiger-mode Avalanche

Photo-Diodes (gAPD, often named Silicon Photomultiplier - SiPM [20]) and Gaseous Photomultipliers (GPM) [21], developed at our group.

The choice between a future LXe or LAr detector is not trivial and is intimately related to the nature of low background rare events detection. The main advantage of LAr, besides its lower cost, is by its efficient discrimination power between nuclear recoils and electronic recoils based on pulse shape. The drawback of LAr is due to lower event rate at smaller energy threshold [4] and the existence of ^{39}Ar isotope in atmospheric Ar [15]. In addition, today's technology does not offer a solution of the direct detection of the Ar $128\,nm$ scintillation photons at cryogenic temperatures. Their detection is currently done using wavelength shifters [22], these have the potential to age or disintegrate in the liquid with time. The issue of the price of the target would eventually become relevant at building a multi-ton scale detector. As a future LXe detector is expected to hold an amount equivalent to the global yearly Xe production, at a price of $\sim k\$/kg$ the price of the detector would be exorbitant.

The study presented here aims at the development of the **Liquid Hole Multiplier (LHM)** - an innovative concept, offering a potential solution for *single-phase*, large-volume noble-liquid TPC detectors of rare events. Although the concept could be applicable to LAr as well, the current study focuses on LXe.

1.5 Liquid Hole Multipliers (LHM)

The **Liquid Hole Multiplier (LHM)** concept (Figure 2) was suggested in 2012 by A. Breskin [23]. It consists of a cascaded structure of thin electrodes perforated with small holes, immersed inside the noble liquid. A thin film of cesium iodide (CsI) is deposited on the top surface of each electrode - serving as a photocathode. The Quantum Efficiency (QE) of CsI immersed in LXe was measured to be ~23% (for an extraction field of $10\,kV/cm$) for the extraction of photoelectrons [24] at $\lambda = 178\,nm$ – the relevant wavelength for liquid xenon emission.

The perforated LHM electrode can be, for example that of the THick Gaseous Electron Multiplier (THGEM) (Figure 3), proposed by R. Chechik and A. Breskin [25]; other electrodes like that of the Gaseous Electron Multiplier (GEM) [26] etc. could be adequate as well. A THGEM is typically a sub-mm thick insulator (typically FR4) with copper deposited on both sides. A hexagonal array of holes (with typically sub-mm diameter and pitch) is drilled and rims are chemically etched around the edge of the holes (Figure 2). Applying voltage across the two layers of copper (typically few hundred volts in gas at atmospheric pressure) results in a dipole-like field inside the holes, reaching values as high as few tens of kV/cm. Detectors based on the THGEM concept have been developed for particle tracking [25], neutron imaging [27], UV-photon imaging in Cherenkov detectors [28] [29] and more recently for gaseous photomultipliers (GPM) operating at cryogenic temperatures [30] [31] [21]. The latter are currently developed in our group as potential photo-sensors in future noble-liquid TPCs.

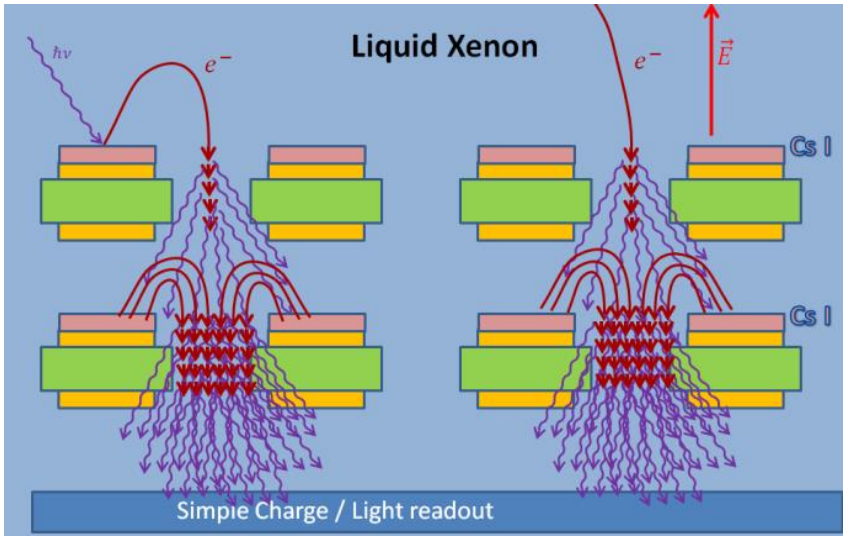

Figure 2 LHM operation principle. Left: A UV photon extracts a photoelectron from the CsI layer deposited on a THGEM electrode. The photoelectron, drifting in a high field region inside the hole creates further electroluminescence, causing the emission of additional photoelectrons towards the next THGEM. The process can be repeated by cascading multiple elements. Charge or light is recorded at the last stage. Right: an ionization electron drifting in an electric field, is focused into a THGEM hole and induces a similar photon-assisted amplification process.

The LHM mechanism is shown in Figure 2. A radiation-induced scintillation (S1 or S2) photon impinging on the CsI photocathode (deposited on the top THGEM electrode) causes photoemission of an electron; the latter drifts along the field lines into the nearest THGEM hole. It was suggested in [23] that under a sufficiently high electric field within the hole, the electron will further excite the liquid atoms, leading to the emission of photons by an electroluminescence process [32]. A second CsI-coated THGEM electrode underneath would convert these photons to photoelectrons and initiate a similar amplification process. Stacking several CsI-coated THGEMs would thus result in the amplification of a single photon into a detectable "*photon flash*"; the latter can then be recorded by a photo-sensor. In principle, the charge induced by the electron cloud photo-emitted into the last stage of amplification (THGEM holes), could be detected on charge-readout elements. (see Figure 2).

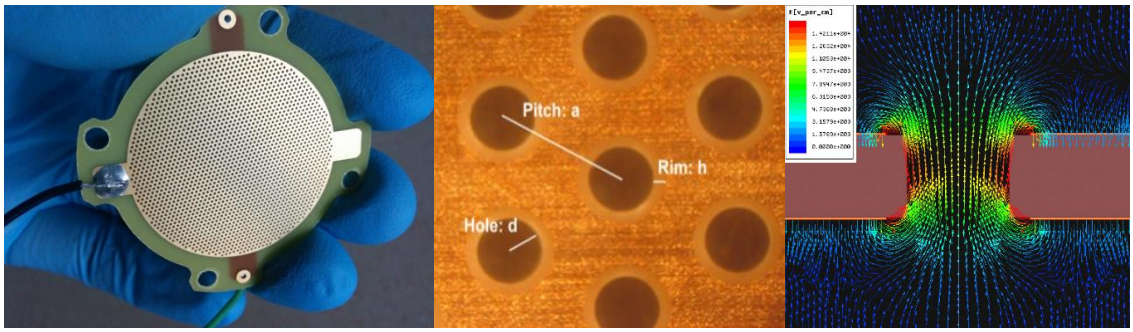

Figure 3 Left to right: Picture of a 35 mm diameter THGEM electrode. A THGEM electrode under the microscope. Electrostatic simulation of the electric field inside a THGEM hole.

Similarly to the scintillation photons, radiation-induced ionization electrons originating at the site of interaction, would drift (under an electric field) towards the THGEM cascade.

They would be focused into the holes and induce the same photon-assisted amplification process described above.

Such an LHM structure would thus offer an elegant solution for a single-phase time projection chamber, enabling the detection of both prompt scintillation at the site of interaction and the detection of the associated ionization electrons.

The assumed feasibility of the LHM concept is based on the following studies that have been conducted in the past:

- CsI photocathodes have high quantum efficiency for the extraction of photoelectrons in liquid xenon at the relevant wavelength - 178 nm [24] [33].
- Moderate charge gain [34] [35] and electroluminescence [36] [37] have been measured in LXe on few-micron thin wires.
- Electroluminescence was recently demonstrated inside THGEM holes immersed in liquid Ar [38] [39].
- The concept of photon-mediated amplification in a cascaded hole-structure in gas was already demonstrated by WIS and Coimbra [40] and by BINP [41] colleagues.

1.6 First trial for electroluminescence in THGEM holes

At the heart of the LHM amplification process is the electroluminescence in the immersed THGEM holes. First steps towards proving its feasibility were done in our laboratory prior to my thesis work [42]. The setup used for the studies is shown schematically in Figure 5. It included an ^{241}Am alpha source placed $5\ mm$ above a THGEM (gold plated electrodes, $0.3\ mm$ hole diameter, $1\ mm$ hole pitch, $0.4\ mm$ thickness, $0.1\ mm$ etched rims around the holes), a 90% transparent mesh electrode placed 2.5mm below the THGEM and a 2'' diameter Hamamatsu R6041-06 UV-sensitive PMT below the mesh. The setup was immersed in liquid xenon inside a large dedicated (WILiX) cryostat, schematically shown in Figure 4 below. Alpha-particles stopped near the source induced primary scintillation photons; a small fraction of them, passing through the THGEM electrode's holes, yielded the primary scintillation signal (S1). Alpha-induced ionization electrons drifted towards- and caused electroluminescence in the THGEM holes; the resulting (S2) signals were recorded using the same PMT.

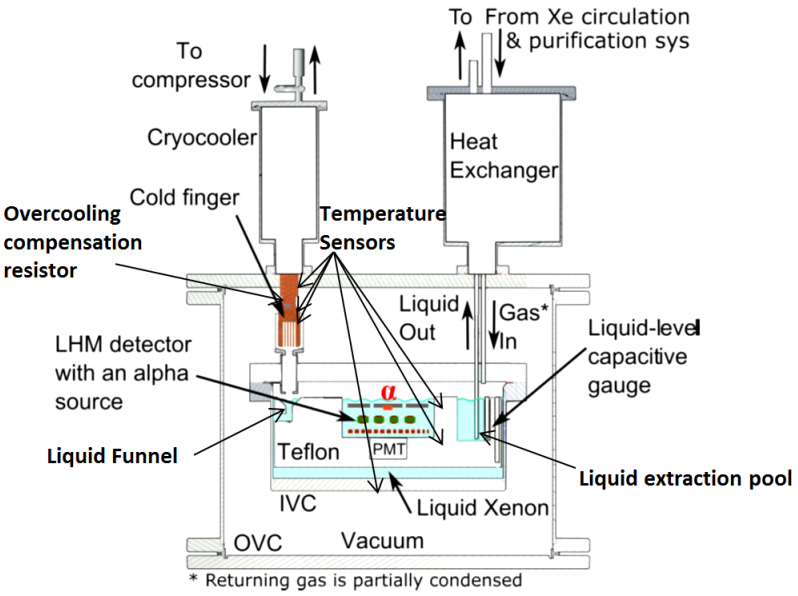

Figure 4 Schematics of the cryogenics of WILiX: cold finger cooled by an external compressor, funneling of the liquid to the side where it flows to the bottom and fills in the central volume of xenon, liquid extraction pool and heat exchanger, 3 temperature sensors along the cold finger, 2 temperature sensors in the main Teflon block, a temperature sensor at the bottom of the chamber and liquid level capacitive gauge. Adapted from [42].

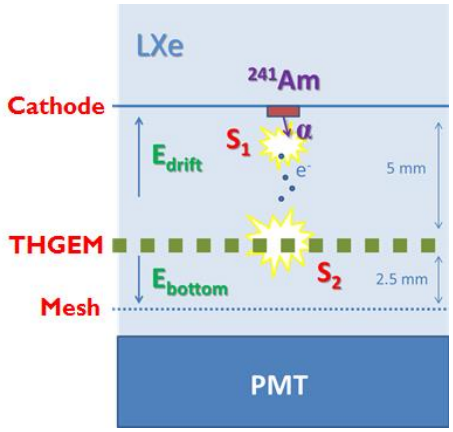

Figure 5 Schematic view of the LHM-studies setup. It includes a biased ^{241}Am alpha source, a bare THGEM (without CsI) and a mesh. The PMT below the mesh records both a fraction of S1 prompt scintillation (through the holes) and S2 electroluminescence in the THGEM holes (from [42]).

The data, published in [42] and shown in Figure 6 suggest, as expected from electroluminescence process, a linear relation between the electroluminescence in the THGEM holes and the electric field (which, in turn is linearly dependent on the applied high voltage across the THGEM electrode). However, the onset of luminescence at $\sim 500\,V$ (corresponding to a field of $\sim 10 kV/cm$ in the THGEM hole) seemed to lie at apparently too low fields, especially considering the measured values of several hundred of kV/cm as suggested in [43] for studies on few-micron diameter wires. These values for the fields are nevertheless well above the reported $2.28\,\mathrm{kV/cm}$ threshold for scintillation at 1.3 bar of GXe [11]. This data raised the suspicion that our hypothesis of the electroluminescence process occurring within the liquid phase might be erroneous. Instead, we came to suspect that electroluminescence is in fact occurring in xenon bubbles located underneath the

THGEM electrode or within the holes. An extensive series of systematic studies was thus launched, using WILiX, to further investigate this new hypothesis; in addition, a new LXe setup (MiniX) was designed to allow for additional directions of investigation as will be described below.

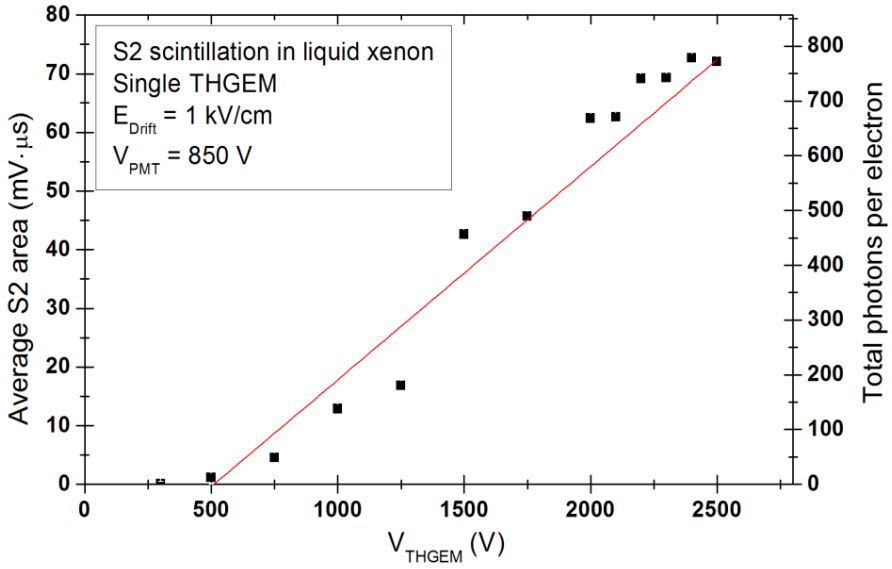

Figure 6 S2 electroluminescence inside THGEM holes as a function of the voltage applied on the THGEM. Data recorded using a Hamamatsu R6041-06 PMT and a non-spectroscopic ^{241}Am source. From [42].

2. Experimental Setups

2.1 The large Liquid Xenon R&D facility - WILiX

WILiX – the Weizmann Institute Liquid xenon facility (schematically depicted in Figure 4) is a large R&D playground, dedicated for liquid-xenon based detectors. The heart of the system is a multipurpose ultrahigh-vacuum chamber with the LXe TPC vessel surrounded by vacuum thermal insulation.

The liquefaction of xenon is done on a cold finger cooled by a Joule-Tompson cryocooler (Brooks Automation PCC) and a $50W$ Proportional-Integral-Derivative (PID) feedback loop controlled heating resistor to compensate for the overcooling. The liquefied xenon drips from the cold finger into a funnel inside the main Teflon block in the xenon chamber. The liquid is then funneled to the side of the chamber, flows to the bottom and fills in the central region. Once the liquid exceeds a level determined by an external manipulator, it pours into an intermediate "pool" where it is sucked out through a heat exchanger to the purification system. The liquid evaporates already inside the heat exchanger; the cold Xe gas is transferred using a recirculation diaphragm pump (Air Dimensions R061-FN-CB2-D) through a mass flow controller (MKS 1479A) to a hot getter (SAES PS4-MT3-R-2); the purified gas returns through the heat exchanger to the chamber partially condensed. The chamber's pressure is measured using a capacitive manometer (MKS 722B). Temperature sensing is done at four points along the cold finger, two points inside the Teflon block and one on the outer bottom part of the xenon chamber (see schematics in Figure 4). The liquid level is sensed using a capacitive gauge. The PID feedback loop supplies current to the heating resistor in order to stabilize the temperature of the liquefaction fins. Consequentially, the sole control over the temperature, and thus the pressure of the liquid in the vessel, is by tuning the set point of the control loop of the liquefaction fins.

The central region of the PTFE block housed the LHM setup, shown in Figure 7. The LHM electrode in this work was the same unit used in [42]: a round THGEM with an active diameter of $34\ mm$, consisting of a $0.4\ mm$ thick FR4 substrate with an hexagonal array of $0.3\ mm$ diameter drilled holes of $1\ mm$ pitch, surrounded by $0.1\ mm$ etched rims. The $20\ \mu m$ copper clad on the two faces of the THGEM was gold-plated. The THGEM was held in place by PTFE spacers, as shown in Figure 7. A non-spectroscopic $16.4\ kBq$ ^{241}Am source with an active diameter of $4\ mm$ was held face down above the THGEM. The distance between the active surface of the source and the THGEM top face was $3.8\ mm$. The source was fixed on a stainless steel holder with HV bias, $\sim 3\ cm$ below the liquid-gas interface. A set of holes in the source holder plate allowed LXe circulation through the LHM assembly. The voltage difference between the source holder and the top face of the THGEM defined the drift field, E_d. An electro-formed copper mesh with 90% transparency (Precision Eforming, MC17), consisting of a square grid of $18.5\ \mu m$ wires with a pitch of $0.34\ mm$ was installed 2.5 mm below the THGEM; the voltage difference between the THGEM bottom face and the mesh defined the transfer field, E_t. All four surfaces – source holder, THGEM top, THGEM bottom and mesh were biased separately using a CAEN N1471H HV power supply. Light signals were recorded by a Hamamatsu R8520-06-Al-MOD PMT (S/N LV0029, QE of

22.4% at $175\ nm$) located $6\ mm$ below the mesh. The PMT was biased at $600\ V$, ensuring operation in its linear regime over the range of S2 signals observed. The PMT signals were fed directly (without amplification) into a digital oscilloscope (Tektronix 5054B); recorded waveform (an example shown in Figure 8) files were processed off-line with dedicated software tools developed for this purpose. The typical sampling rate was 250 MS/s, with an acquisition rate of ~1000 frames (waveforms) per second.

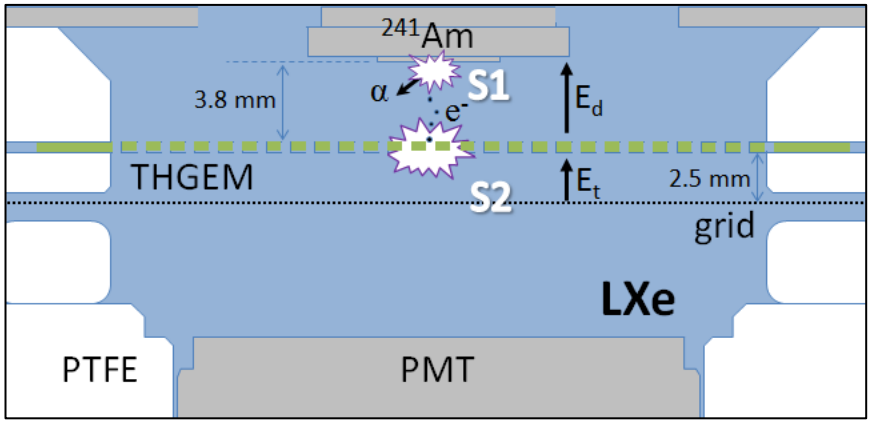

Figure 7 Schematic drawing of the LHM setup. The main components are drawn to scale. Alpha particle emissions into the liquid result in prompt scintillation light ("S1"). Ionization electrons liberated from the alpha particle track drift towards the THGEM where they induce secondary scintillation ("S2") inside the holes. UV light is recorded by a bottom PMT. The liquid level (not shown) is ~3 cm above the ^{241}Am source.

Since the 5.5 MeV Alpha-source used in this experiment is non-spectroscopic, the particles leave a fraction of their energy in the source's protective matrix; this is reflected in the low-energy tail of the spectrum of the source, recorded with a Si surface-barrier detector, as seen in Figure 9. The mean residual energy is of ~4 MeV. The alpha decay of the ^{241}Am only rarely ends directly on the ground state of ^{237}Np (0.4% of all decays); this leads to further emission of gammas and conversion electrons before complete relaxation. 36% of the alpha decays are accompanied by a $59.5\ keV$ gamma photon. Other decay channels involve lower energy gammas and conversion electrons, or higher energy gammas with vanishing probability, all of which are negligible in this study [44]. Depending on the angles of the emitted particles from the source, events in the liquid might show a coincidence of alpha and gamma/electrons, only alpha or only gamma/electrons.

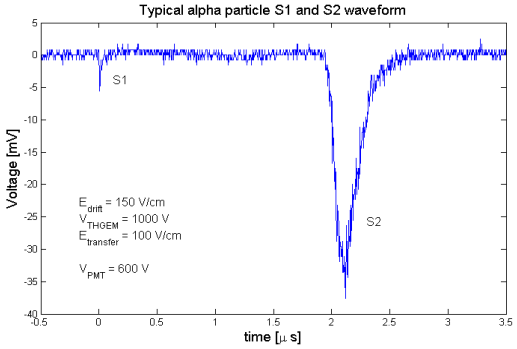

Figure 8 Typical S1 and S2 waveform from an alpha particle recorded by a PMT located underneath the THGEM. Electric field in the THGEM holes: ~ 15kV/cm.

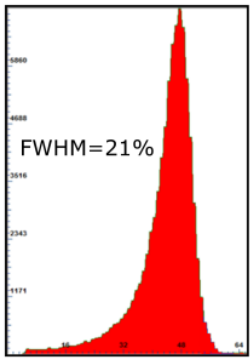

Figure 9 ^{241}Am non-spectroscopic source; alpha-particle spectrum measured using a silicon surface-barrier detector. From [42].

2.2 New liquid xenon R&D facility – MiniX

2.2.1 Motivation and desired specifications

Our first investigations of the LHM properties, performed in WILiX, has suffered from a too long turnaround; this large-volume research facility, originally planned for gaseous photomultipliers studies with a LXe TPC, has typically 10 days cool-down and thermodynamic stabilization time. Therefore, we found it necessary to design an additional smaller cryostat system – dedicated to the LHM studies, which will allow for quick modification in the LHM electrode configurations.

The newly designed within the framework of this thesis, and already operating, MiniX cryostat has a smaller size; it permits investigating the properties of detector elements of ~30mm diameter, located within a LXe TPC-like volume of about 70mm diameter x 100mm length. The philosophy behind the design was: to aim for a short turnaround time with a flexible modular structure allowing for easy exchange of inner detector parts. Furthermore, since CsI, the photocathode material, is sensitive to environmental conditions, the detector assembly was designed to fit into a nitrogen glove-box with quick transfer into the cryostat chamber, with minimal exposure to air.

MiniX's schematic view is shown in Figure 10. The liquid xenon chamber is a 4'' diameter $250\,mm$ long $0.7\,mm$ thick stainless steel cylinder, sitting inside the Outer Vacuum insulation Chamber (OVC). $150\,mm$ above its bottom, a copper ring is silver-soldered to its outer circumference. The ring is cooled down with liquid nitrogen, as described below, allowing for the liquefaction of xenon. While the entire volume is filled with xenon vapor, only the lower 150mm are filled with liquid xenon. The upper part of the cylinder is connected to a 6'' diameter 8-way turret, having service ports for the various functions. Some of the inner parts within the liquid-xenon volume (*fixed parts*) are located inside a PTFE cylinder at the bottom of the chamber and are subject to less frequent changes. These include a capacitance liquid-level meter (American Magnetics Model 286 with custom made capacitor sensor), a Pt100 temperature sensor (Lakeshore PT111), the liquid outlet tube, a photomultiplier tube (Hamamatsu R8520-06-Al) facing upwards and a mesh to protect the PMT and to define relevant fields within the detector. Power, signal, and high-voltage are supplied to- and extracted from- the *fixed parts* using the 2.75'' CF feedthroughs on the

upper turret (high voltage feedthrough: Solid Sealing Technology FA14101-04, 3x coaxial BNC feedthrough: Solid Sealing Technology FA14949 and low voltage feedthrough: Accuglass MIL-C-26482). The *detector assembly*, mechanically decoupled from the *fixed parts* is suspended from the top most 8'' CF flange. All parts of the *detector assembly*, including voltage supplies and signal outlets, are connected to feedthroughs on the top most flange (high voltage feedthrough: Solid Sealing Technology FA14101-04, 3x coaxial BNC feedthrough: Solid Sealing Technology FA14949); this enables a quick and easy mounting into the chamber once the detector is assembled (particularly with a CsI photocathode) in a nitrogen glove box.

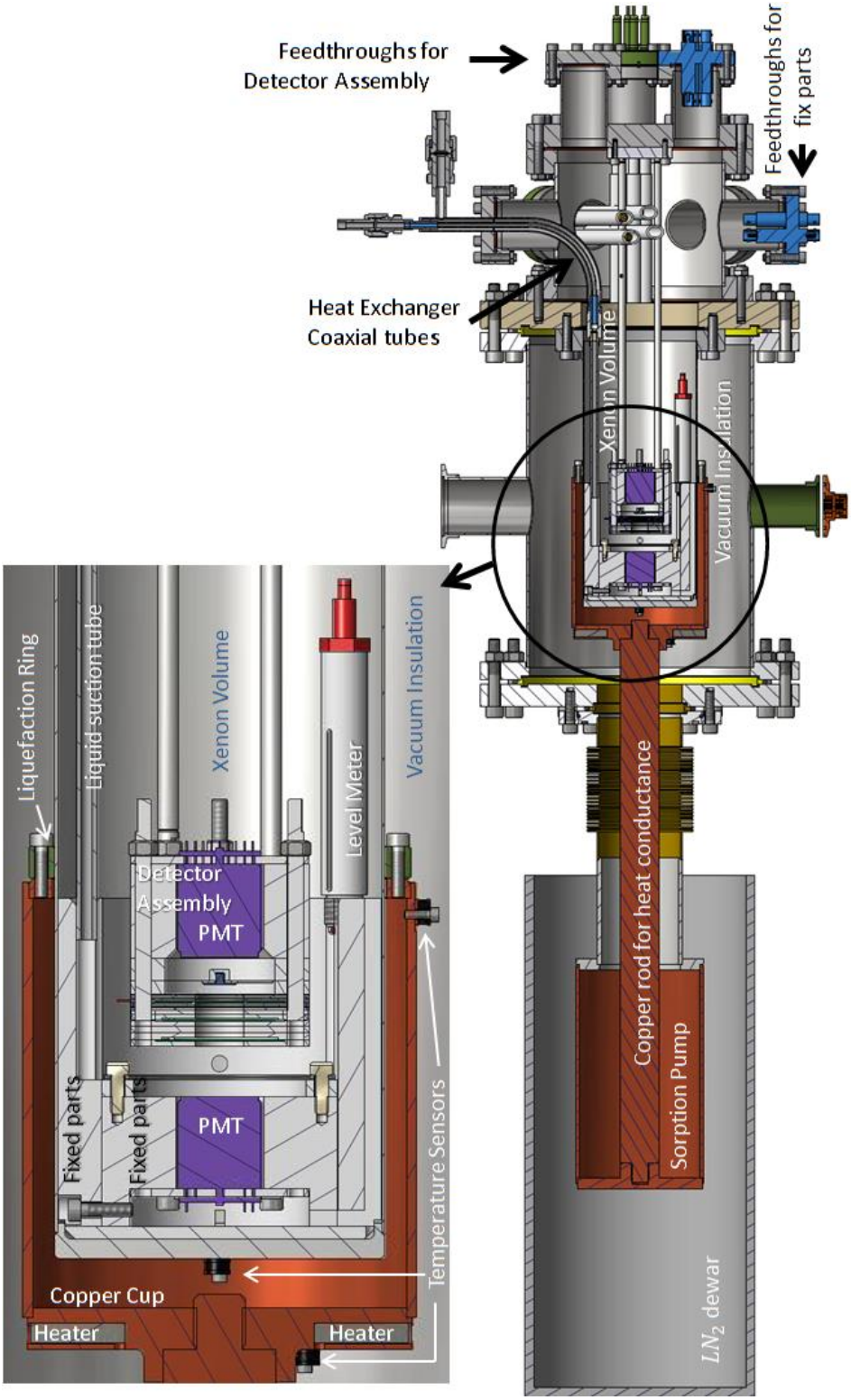

Figure 10 Cross section of the MiniX cryostat. An expanded view of the *Detector assembly* is provided below (Figure 12).

2.2.2 Cryogenics and thermodynamics control

MiniX cryogenics is based on liquid nitrogen cooling. The bottom part of the Outer Vacuum insulation Chamber (OVC) is a copper cup; it is immersed during operation inside a liquid nitrogen-filled dewar. A $500\ mm$ long copper rod is connected (by a thread) to the OVC on

its bottom part, thermally coupled by Apiezon-N grease. The top end of the rod is screwed into a base of an internal copper cup (surrounding, but not touching the liquid xenon volume) cooling down the cup's base. The top part of the copper cup is screwed the copper ring, silver-soldered onto the outer circumference of the stainless-steel chamber containing the liquid xenon (see Figure 10). Heat load from the incoming gas and heat leaks from the environment (due to conduction through body materials, through the Xe gas and due to radiation) as well as the desired working temperature dictated the dimensions of the rod and the inner copper cup. Overcooling is compensated by a feedback-loop-controlled 50Ω resistor (CryoCon 3039-001 cartridge heater) located at the bottom of the inner copper cup (see Figure 10), allowing for the accurate control of the ring temperature. The temperature is measured both at the bottom of the copper cup and at the ring by two CryoCon S900-BB Silicon diodes, read out by a CryoCon Model 24C which supplies the current (up to $1\ A$) for the heater control loop. Other temperature sensors are located at the bottom of the LXe chamber and inside the *fixed part*'s PTFE cylinder measuring the liquid temperature. Vacuum for thermal insulation is maintained either by continuous pumping of the OVC or by introducing molecular sieve in the bottom copper cup turning it into a sorption pump. The inner chamber is wrapped with super-insulation (aluminized Mylar sheets) to reduce heat load due to radiation.

The gas manifold is schematically depicted in Figure 11. Xenon gas, stored in a 2L sampling cylinder at $\sim 50\ bar$ (at room temperature), is transferred through a pressure reducer (Matheson SEQ93074V4MM) and a hot getter (SAES PS3-MT3-R-2) into the chamber. The gas liquefies on the coldest part of the walls, namely were the copper ring encompasses the xenon chamber (Figure 10). The liquid fills in the chamber, cooling down all inner parts. Once the filling is completed to the desired level, the liquid extraction becomes possible for purification. The liquid is transferred, through the inner tube of a two coaxial tubes heat exchanger, out of the chamber were it evaporates; the gas is transferred using a recirculation diaphragm pump (Air Dimensions R061-FN-CB2-D) through a mass flow controller (Aalborg GFC17S-VCL2-AO), through the hot getter for purification. The gas returns to the chamber through the outer tube of the coaxial heat exchanger, where it is pre-cooled. Pressure in the chamber is measured using a capacitance pressure transducer (MKS 722B). A pressure relief valve (Ham-Let H-985-SS-N1/4-SL-EP) protects the system from over pressurizing by discharging gas into a pre-evacuated 500L aluminum tank, in case of loss of cooling power. The gas manifold includes an input port for argon or nitrogen gas for the assembly of a detector under constant flushing of the chamber. Temperatures, pressure, liquid level, recirculation flow, heating power and liquid nitrogen filling are continuously recorded using dedicated LabView code. Recuperation of xenon both from the chamber and after discharge to the emergency volume is done by cryo-pumping the gas into the sampling cylinder cooled to liquid nitrogen temperature.

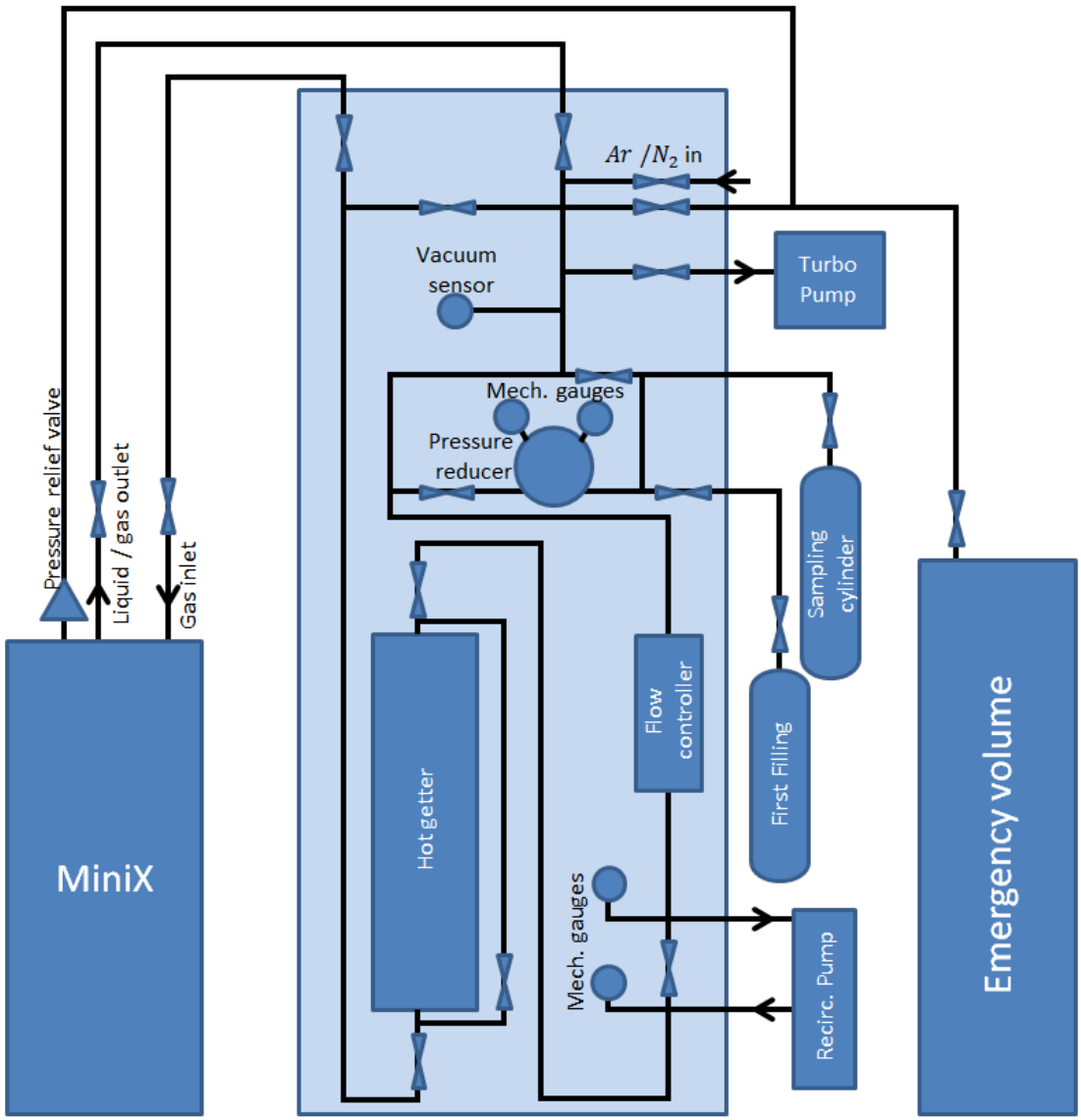

Figure 11 schematic view of MiniX gas manifold.

2.2.3 The detector assembly

MiniX was originally planned to investigate the idea of LHM, a cascaded structure of CsI-coated hole-multipliers able to record both scintillation photons and ionization electrons in a single phase TPC detector. The setup planned, shown in Figure 12 consists of a top PMT facing downwards serving as a trigger, an ^{241}Am alpha source, three CsI-coated THGEMs held between Teflon holders and spacers, a bottom mesh and a bottom PMT. Electrical contacts are made using U-shaped clips to enable quick and easy assembly inside a nitrogen glove box. Similar to the above described LHM setup Figure 5 , alpha particles emitted from the americium source are stopped in the liquid within $\sim 30\ \mu m$; scintillation photons reflected from the Teflon holders of the first THGEM serve as trigger at the top PMT (with estimated photon detection efficiency of 4% using a GEANT 4 simulation). Photons hitting the CsI photocathode and ionization electrons participate in the amplification process as described above.

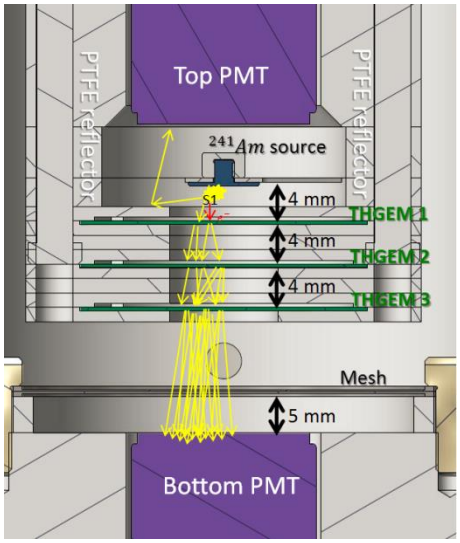

Figure 12 Example of a triple-THGEM LHM setup. The setup consists of a top trigger PMT facing downwards detecting photons reflected from PTFE THGEM holder. ^{241}Am alpha particles induced scintillation photons and ionization electrons participate in the amplification at a cascaded structure of three THGEMs. The final pulse is recorded on the bottom PMT. A mesh protects the PMT from discharges and defines the field underneath the last electrode.

The LHM concept, as explained earlier, can make use of GEM electrodes as well as THGEMs. A GEM, due to its thinner geometry (its insulating substrate is typically $50\ \mu m$ thick), allows reaching higher fields in the holes than a THGEM, with a potentially higher photon yield due to electroluminescence (possibly also in the liquid phase itself). A setup was thus also designed to hold a triple-GEM detector. Electrode holders and spacers made of PEEK (Polyether ether ketone) were designed to hold a GEM with a tailored design in place. The holders allowed a fold in the GEM at their outer circumference such that the clip depicted in Figure 13 can be inserted for electrical contact.

Figure 13 A triple-GEM configuration. Each GEM is held between two PEEK-made holders. Electrical contacts are made by folding the thin GEM foil over the PEEK holder and attaching a clip connected to high voltage feedthrough.

2.2.4 G-MiniX – looking into the xenon

In addition to the indirect studies of the bubbles-assisted electroluminescence in holes within liquid xenon, modifications of the MiniX system design are planned to allow for optical recording of the bubbles. The aim was to allow for the study of bubble formation and its potential control. Figure 14 shows the setup designed for this purpose. Two windows were added, an external one, directed into the OVC, and an internal one between the OVC

and the inner xenon volume. They were designed to allow observation of the central part of the detector electrode with a dedicated optical system. In addition, a frame onto which resistive wires are stretched is located underneath the THGEM electrode; passing current through the wires results in heating and consequentially in creating bubbles, which would subsequently deposit under the THGEM electrode. A commercial long-working-distance magnifying lens and a high definition camera system (CALTEX VIP-50-HD60) will enable focusing both on the THGEM bottom and on the wires. A second heating-wires frame is designed to replace the original bottom mesh, in case the bubbles generation on the nearby wires disturbs photographing the THGEM electrode. (The detector assembly is shown in Figure 14)

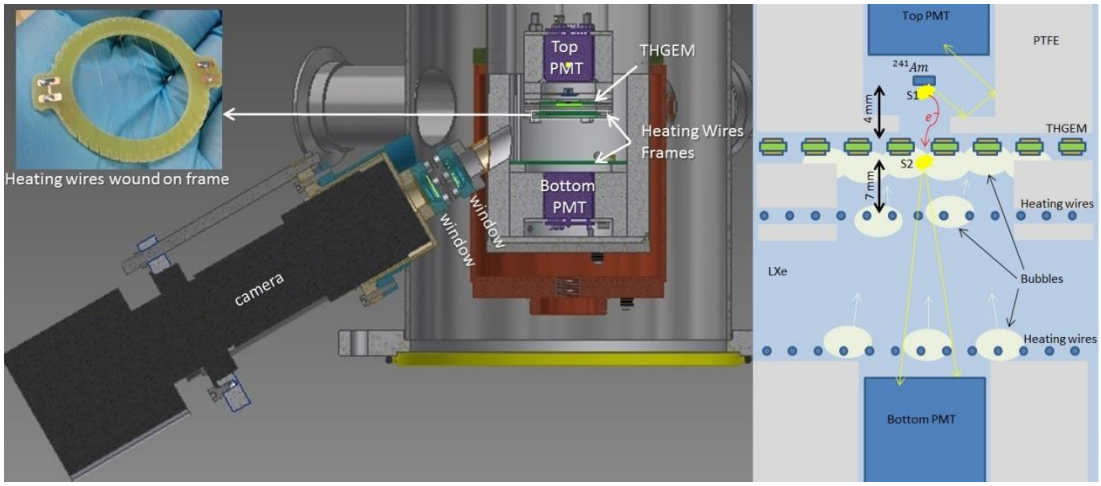

Figure 14 Two windows (light blue) allow for looking onto the bottom of a THGEM (or GEM) (light green) in the detector assembly. Two heating-wire frames (dark green) allow for the creation of bubbles in the liquid. The expanded scheme is provided to the right.

3. Results in WILiX

3.1 Bubbles hypothesis validation

Our first goal towards the validation of the LHM concept [23] by a systematic R&D program was to understand the reason for the copious photon yield observed in the preliminary study [42], at apparently abnormally low electric fields. As noted above, a leading hypothesis was electroluminescence within xenon bubbles trapped under the THGEM holes [45] [46]; these bubbles are presumably generated, when the system is in thermodynamic steady state, on one or more surfaces below the THGEM, whose temperature is slightly higher than that corresponding to the equilibrium between the phases at the given system pressure[1]. Direct observation of bubbles inside the WILiX cryostat was not possible due to the complex geometry of the cryostat system; therefore indirect observations, pointing at the existence of bubbles in the liquid, were necessary. Our expectation was that bubble formation and the ensuing S2 properties would be greatly affected by pressure changes in the system. In particular, it was expected that a step increase in the pressure will make the S2 signals disappear as a result of bubble collapse. Thus, an experiment was set to measure the rate of S2 signals during and following such pressure changes.

The S2 rate measurement setup is shown schematically in Figure 15. The signals from the PMT were split in two: one line into the oscilloscope (Tektronix TDS5054B) for waveforms acquisition, and the other to a Timing Filter Amplifier (TFA - Ortec 474) leading to a Constant Fraction Discriminator (CFD - Canberra 1428) and from there to a scaler (Counter input of a NI-DAQ USB60008 card); the latter was read out with a LabView code. Voltages in the detector assembly of Figure 7 were set constant for the entire duration of this measurement: a nominal drift-field $E_d = 130\,V/cm$, $V_{THGEM} = 1250\,V$, $E_t = 1\,kV/cm$ and $600\,V$ on the PMT.

[1] For a bubble to grow, the internal pressure inside the bubble should overcome the force exerted due to the surface tension of the liquid. For example, for a $1\,mm$ diameter bubble to grow at $170\,K$ (corresponding to a vapor pressure of $1{,}334\,mbar$), the excess pressure inside the bubble should be at the order of $0.4\,mbar$ [55]. A temperature difference in the liquid smaller than 0.1K supports this pressure difference. Therefore, in order for bubbles to be created only a tiny temperature gradient is needed. This however should be taken with a grain of salt, as this calculation does not take into account the detachment of the bubble from the surface.

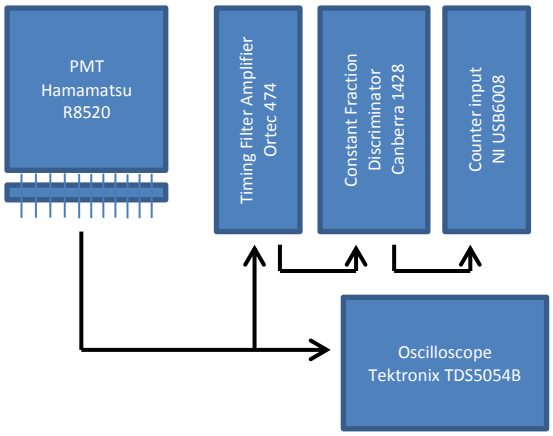

Figure 15 Schematics of our setup for counting S2 signals produced in THGEM holes in the setup shown in Figure 7. The PMT signals are split into the oscilloscope and a timing filter amplifier. The amplifier signal is transferred into a constant fraction discriminator and to a counter input of a NI-DAQ card. Read out is done by a dedicated LabView code.

Inducing a step increase in pressure was done by increasing the temperature of the liquefaction fins (by 10 degrees from 163.0K to 173.0K). Figure 16 shows the temperature of the cold finger cooling fins (A), the xenon pressure (B), the chamber's bottom temperature sensor (C), the overcooling compensation heater power (D) and the S2 trigger rate (E) as a function of time during and following a step increase in the fins temperature. First, it is clearly seen that shortly after the rise of the fins temperature, the rate of S2 triggers dropped to zero (~1 minute after the change). Second, once the S2 triggers reappeared (~13 h later), it happened abruptly. Our physical interpretation is as follows: the step increase in the cold finger temperature induces a rapid increase in the gas temperature and pressure; this, in turn, results in a simultaneous increase in the liquid pressure. Bubbles, trapped underneath the THGEM (and serving as the medium for electroluminescence), collapse and disappear when the liquid pressure exceeds their vapor pressure (more precisely – when their vapor pressure can no longer support the combination of surface tension and increased external pressure), leading to the disappearance of S2. Since the heat capacity of the inner chamber components is large (their total mass, including the PTFE block, LXe and stainless steel parts exceeds 20 kg), it takes many hours for the temperature to increase and stabilize on its new steady state value. At some point (here, ~13 h after the step increase in pressure) the temperature of the surface (or surfaces) which generate the bubbles becomes high enough to allow bubbles to grow and detach from it, subsequently reaching the THGEM bottom and leading a resumed electroluminescence.

Furthermore, at normal operation (when there is constant boiling on the bubble-generating surfaces), the rate of S2 triggers fluctuates (Figure 16E). These fluctuations are attributed to instabilities in the S2 waveform pulse-height and are also seen by eye when looking at the oscilloscope. It was surprising to see that once the S2 signals reappear (at t=15.8 h in Figure 16J), there is a regime lasting ~1.5 hours where the S2 rate is completely stable; following that, it returns to the usual fluctuation regime (at t=17.3 h). The transitions between these three stages, namely from the non-boiling (no S2) regime to the 'super-stable' S2 regime and then to 'normal boiling' (fluctuating S2) regime, are coincident with small step increases in the gas pressure and with step drops in the power provided by the heater to keep the cold fins at 173 K. This is an indication that both transitions are accompanied by increased heat

transfer from the bubble-generating surfaces to the liquid; a possible explanation for the second step is that at this point an additional surface reaches the threshold temperature required for bubble formation. A third power drop (at t=19.7 h), correlated with a 'waist' in the S2 trigger rate and another slight increase in the pressure, may indicate that a third surface starts contributing to bubble formation.

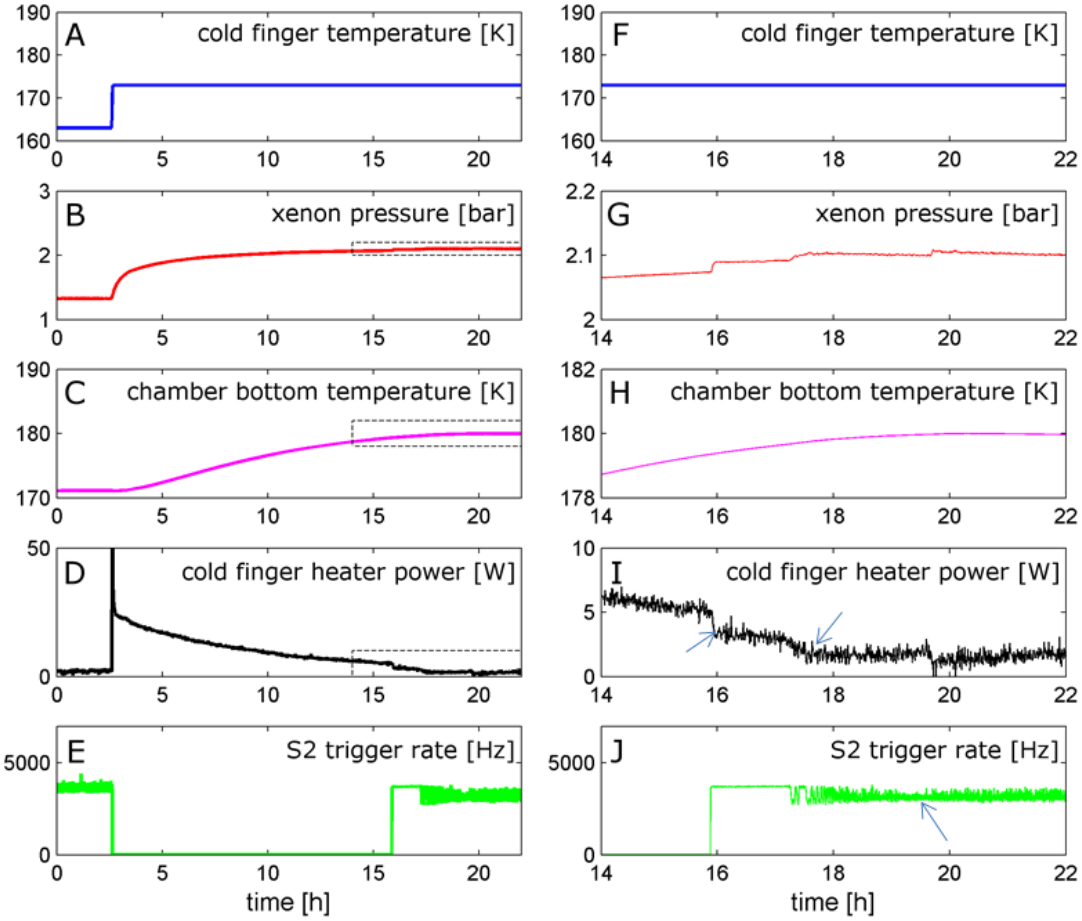

Figure 16 Variation of system parameters causing- and associated with the disappearance and reappearance of S2 signals (E) (S2 trigger rate) after a step increase in the cold finger's temperature (A). The plots on the right column are on an expanded view, magnifying the S2 pulses reappearance period (dotted rectangle) of the left column. Arrows on (I) show the three decreases in heater power corresponding to the reappearance of S2 and to its destabilization in two steps.

3.2 Study of S2 properties

Having understood that the electroluminescence demonstrated in [42] was not in liquid, as originally foreseen in [23], whetted our appetite to initiate a careful study of this new, unexpected kind of detector – the *bubble-assisted LHM*. The study focused mainly on the parameters affecting the light yield within the THGEM holes and on the reachable S2-pulse resolution as a function of the drift field (E_d), THGEM voltage, transfer field (E_t) (see setup in Figure 7) and pressure in the LXe vessel.

It is first instructive to analyze the complete histogram of all the waveforms acquired in a given set of voltages and thermodynamic conditions. Figure 17 shows a 2D histogram of S1

and S2 waveform areas (time integral of the pulses) recorded at a $0.8\mathrm{kV/cm}$ drift field, $2\ \mathrm{kV}$ across the THGEM and a reverse transfer field of $0.4\ \mathrm{kV/cm}$ (setup of Figure 7) at a pressure of 1.3 bar and a PMT voltage of $600\mathrm{V}$. The histogram shows the main features discussed above of the $^{241}\mathrm{Am}$ source. The central diagonal distribution is associated with the alpha particles (of which a large fraction is in coincidence with gammas and/or conversion electrons). The diagonally elongated shape of this event distribution reflects the qualitative behavior expected from a non-spectroscopic alpha source (average energy $\sim 4\mathrm{MeV}$). The $59.5\ \mathrm{keV}$ line can also be seen in the upper blob of the lower left corner of the figure. Although a factor ~ 70 in energy, the S2 ratio between alphas and $59.5\ \mathrm{keV}$ gammas is only ~ 4. This is attributed to the difference in the charge yield (fraction of ionization electrons escaping recombination) between an alpha particle track and a track of a recoiling electron in LXe[2] [10]. An even lower energy "peak" is seen. These events are composed of several contributions. One is from the overlapping of the $\mathrm{K}\alpha$ and $\mathrm{K}\beta$ escape peaks of xenon (at 29.9 and $25.8\ \mathrm{keV}$ respectively [47]: when a $59.5\ \mathrm{keV}$ gamma photon knocks out an electron from the Xe atom K-shell (which deposits its energy in the liquid), the "hole" is compensated by another electron de-exciting via x-ray emission (with a photon at 29.6 or $33.7\ \mathrm{keV}$); the x-ray photon then has the probability to be reabsorbed on the source plate with no further contribution to S2. Other contributions are due to the lower-energy gammas (13.9 keV, 26.3 keV) and conversion or Auger electrons emitted during the alpha decay chain. The apparent 'peak' structure of these contributions (rather than a falling continuum) results from variations of the smallest pulses crossing the trigger threshold.

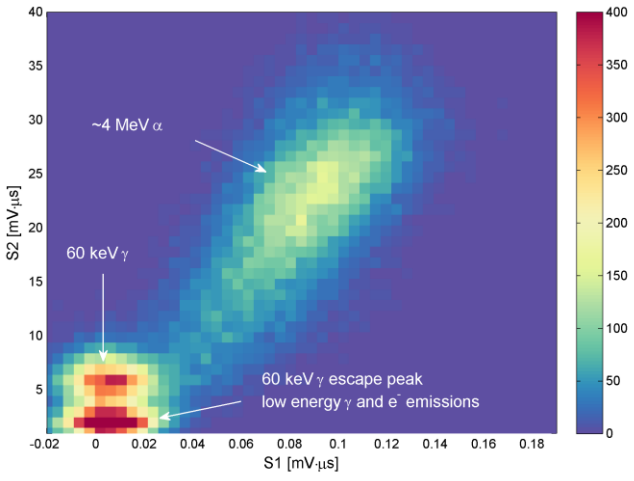

Figure 17 S1 vs S2 2D histogram taken at $0.81 kV/cm$ drift field, $2\ kV$ across the THGEM and a reverse transfer field of $0.4\ kV/cm$, $V_{PMT} = 600V$. The histogram shows the main alpha emission channels of the non-spectroscopic ^{241}Am source: a continuous distribution of alpha particles peaking at $\sim 4\ MeV$ manifested in a large S1 and S2 signals, the associated $\sim 60\ keV$ gamma showing almost no primary scintillation and ~ 4 times smaller S2 than the alpha line and a low energy 'peak' corresponding to low energy gammas and electrons emissions from the source.

[2] For alpha particle tracks, the fraction of electrons escaping recombination is ~2-3% at a field of 1 kV/cm; for 60 keV electrons it is ~60% for the same field [11].

The study presented next focuses mainly on alpha-particle induced events. As is inferred from Figure 17, the selection of the alpha-induced events can be done easily by setting a threshold on the S1 signal's area (the time integral of the pulse shape), which is proportional to the number of photoelectrons arriving at the PMT. In this particular example, setting $S1 > 0.03\ mV \cdot \mu s$ cuts away essentially all of the events in which no alpha particle is emitted into the liquid; in these discarded events ($S1 < 0.03\ mV \cdot \mu s$) the S2 signal comes from either 59.5 keV gammas, or the low-energy emissions of gammas and electrons from the source. Since the source is non-spectroscopic, in order to better estimate the actual properties of electroluminescence spectrum (in particular – the S2 luminescence resolution), one can apply a more restrictive cut on S1, to focus on events in which the alpha particles enter the liquid with energies close to the maximum of the distribution (geometrically, this limits the analysis to alpha particles leaving the source at ~90°). For practical purposes, the choice of S1 threshold cannot be too high, otherwise the number of events passing the cut would be too small. Thus, in what follows, we chose $S1 > 0.1\ mV \cdot \mu$ sec; this choice allows for good statistics at the price of including some events with lower energies, resulting in a somewhat asymmetric S2 spectrum. An additional complication arises from the coincident emission of alpha particles with $59.5\ keV$ gammas or other low-energy emissions from the source. These events cannot be discarded based on S1 cuts and require more careful analysis. When the conversion of the $59.5\ keV$ gamma photon (having an attenuation length of $\sim 0.4\ mm$ in LXe) occurs at a distance from the source, the resulting waveform is composed of two peaks, the first being the gamma photon ionization electrons and then the alpha-induced electrons (see example in Figure 18). If however, the pulses are not well-separated in time, the waveforms of the alpha pulse and of the gamma pulse partially overlap. Discarding them is based on pulse shape cuts. A too long rise time of the pulse or a wide pulse would hint to a coincidence event. Still, events in which the alpha and the gamma have converted close to each other (or events in which the alpha particle is accompanied by low-energy gammas or electron emission from the source), cannot be discarded by pulse shape cuts, leaving some residual smearing in the S2 spectrum. After applying the above cuts, the peak centroid and the variance of the S2 distribution are extracted from a Gaussian fit performed on individual spectra. Because of the residual asymmetry of the source, a one-sided Gaussian fit (to the right side of the peak), gives a still better estimate for the S2 resolution. Figure 19 shows the S2 spectrum acquired in 'super-stable' conditions, with no S1 cut, with a cut requiring $S1 > 0.1\ mV \cdot \mu$ sec and with additional alpha-gamma coincidence cuts. The full spectrum comprises 416,395 waveforms, acquired during ~1 hour of super-stable conditions. The THGEM voltage was $1250\ V$, drift field $0.13\ kV/cm$ and transfer field $1\ kV/cm$ (V_{PMT} = 600 V).

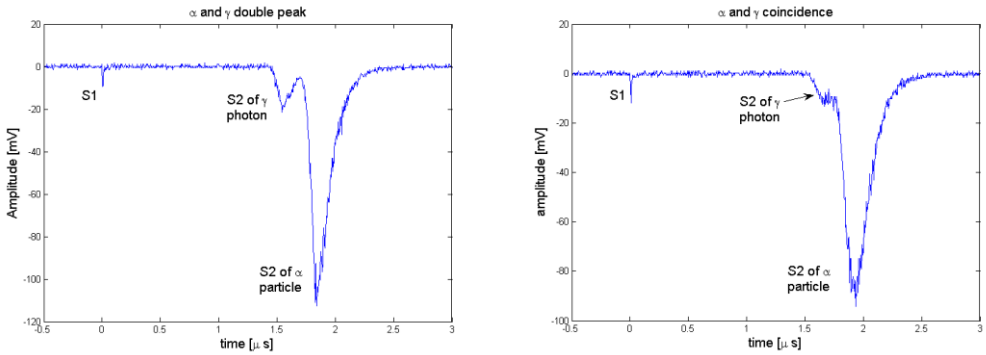

Figure 18 Left: Example of a double peak structure due to alpha particle and gamma photon converted in the liquid. Right: a similar case in which the gamma and alpha pulse shapes partially overlap but can still be discerned.

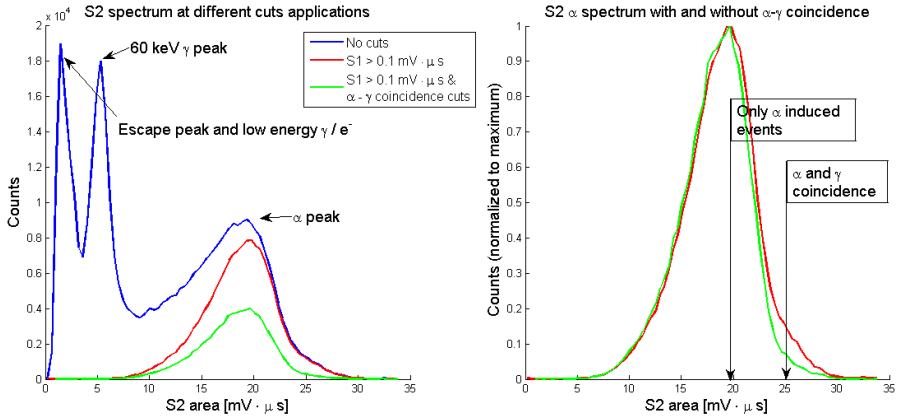

Figure 19 S2 spectra at different cuts application (left figure) for 'super-stable' conditions; high threshold on S1 area removes the lower energy gamma and electron peaks, leaving only the alpha- and alpha-gamma-coincidence events. Right figure: S2 spectra only of alpha particles normalized to their maximum. The red curve shows events after S1 area cut only, the green curve shows the events after both S1 area cut and S2 waveform cuts application. At the pulse area corresponding to the coincidence of alpha and gamma events ($\sim 25\ mV \cdot \mu s$), it can be clearly seen that the S2 waveform cuts are effective for their removal.

It is interesting to analyze Figure 20 which shows the S2 spectrum-centroid as a function of the THGEM voltage during a period of ~3 months at different pressures. Each point relies on ~57,000 waveforms (before applying any cuts), taken over several minutes at a given set of voltages. First, as already demonstrated in [42], the electroluminescence process is, to first order, linear with the electric field. Second, the curves taken at different dates indicate that over this time span, the system showed stable and reproducible results. A rather surprising conclusion however is that the S2 signal does not depend on the pressure in the vessel. This is not expected in an electroluminescence process in gas and the origin to this effect is not yet clear to us (a possible hypothesis is that this reflects a different degree of bubble penetration into the THGEM holes in the two pressure levels studied). The resolution (standard deviation divided by the mean of the distribution) of these curves was also extracted and is seen in Figure 21 below; in this case the resolution is taken from a full Gaussian fit to the alpha particle peak, and not only to its right side.

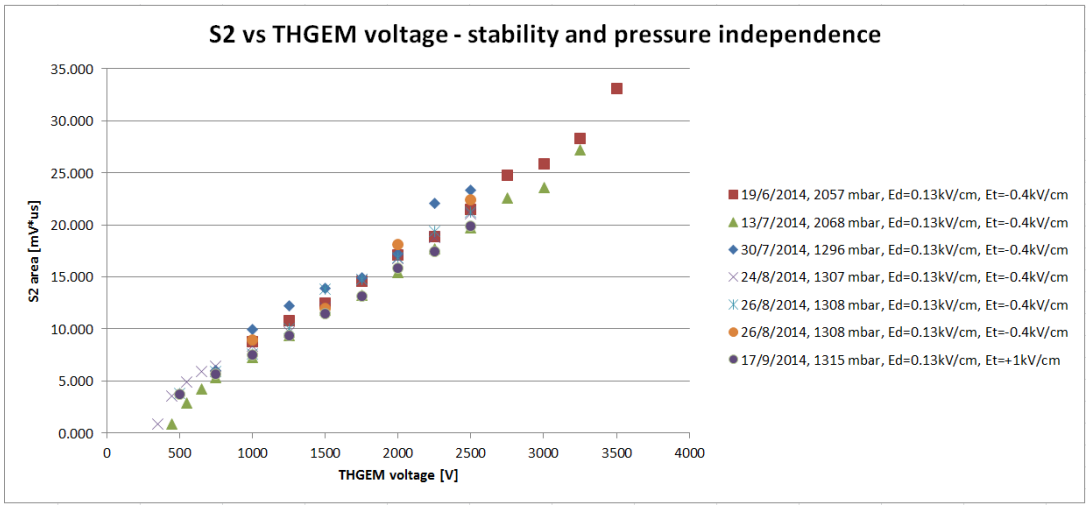

Figure 20 S2-signal–area's centroid as a function of the THGEM voltage. Spectra were taken at $V_{PMT} = 600V$, $E_d = 0.13\ kV/cm$ and a reverse transfer field $E_t = -0.4\ kV/cm$ (all but the last measurement). Over a period of 2 months, the system has shown stable operation and reproducible behavior over time. It is also seen that the electroluminescence is not affected by the pressure.

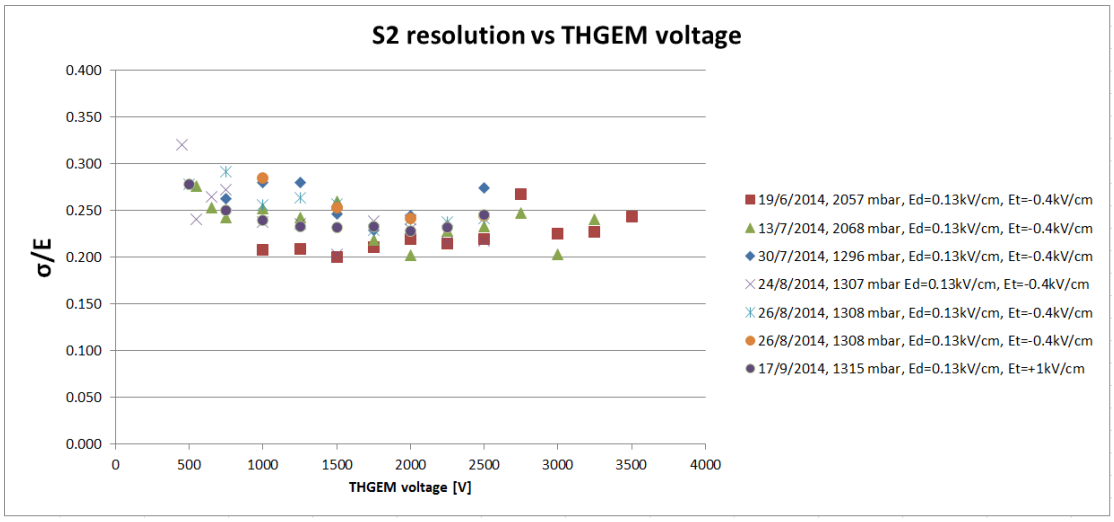

Figure 21 S2 resolution as a function of the THGEM voltage at different pressures and at different dates.

Figure 22 shows the dependence of the S2 pulse area on the transfer field. At negative (reversed) field, the electrons are pushed towards the bottom of the THGEM after passing through the holes (see Figure 23). Starting at zero field, the field lines attract the electrons downwards, qualitatively altering their trajectory. At higher transfer fields, the electroluminescence is extended below the hole to the transfer region. This effect will be discussed in detail below.

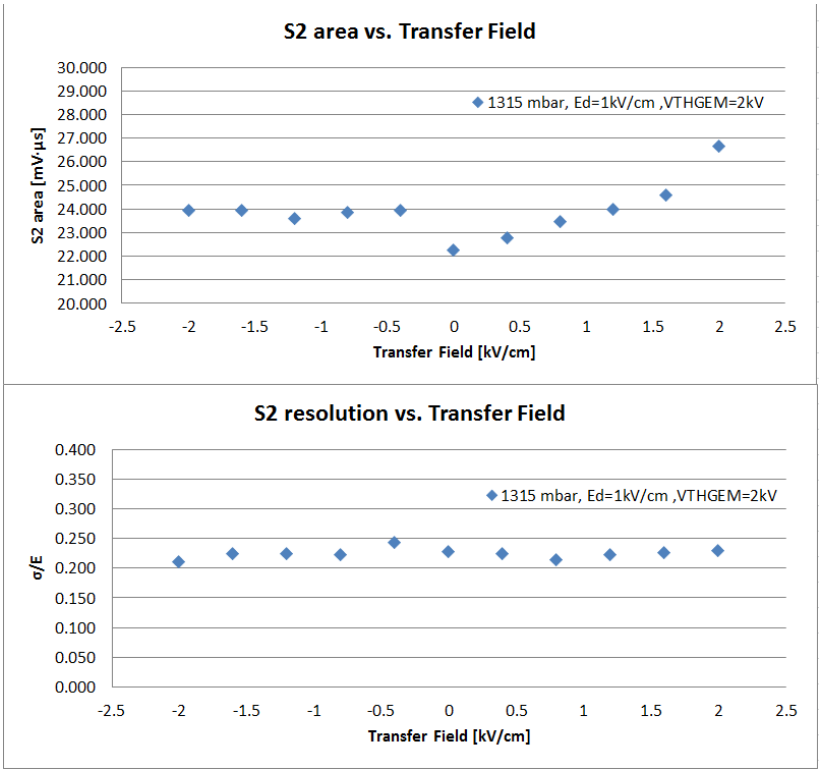

Figure 22 Top: S2 area vs. transfer field. The minimum around zero field is due to the change in the electrons trajectory from drifting to the bottom of the THGEM after passing through the hole to drifting downwards to the mesh electrode. The ~10% increase in S2 at increasing voltage is attributed to further luminescence in the transfer region as will be discussed below. Bottom: S2 resolution as a function of the transfer field.

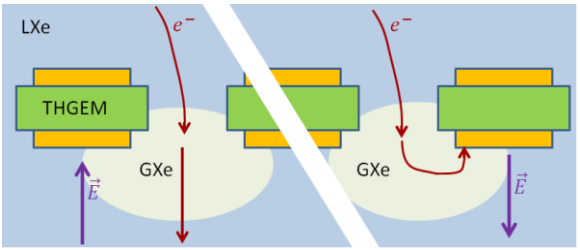

Figure 23 Left: Electron trajectory at positive electric field at the exit from a THGEM hole. Right: electron trajectory at negative electric field after passing THGEM holes.

Figure 24 shows the effect of the drift field on the S2 luminescence in the THGEM holes. The "knee" like structure of the S2 as a function of the THGEM voltage is a result of poor collection of electrons into the holes. The weaker the drift field is compared to the THGEM dipole-field, the better electrons are focused into the THGEM holes at lower THGEM voltages. For a given drift field, the larger the THGEM voltage is, the better electrons are focused into the holes (due to the dipole field which extends further into the drift region). The same effect is seen for the resolution of the peak. At low THGEM voltages, many alpha-particle events result in partial collection of the ionization electron into the THGEM holes, resulting in considerable smearing in a broader S2 distribution. At high THGEM voltage, once the focusing effect is no longer relevant, a larger drift field results in a larger light yield. This

is due to an increase of the number of electrons escaping recombination at the site of interaction at larger electric fields [10].

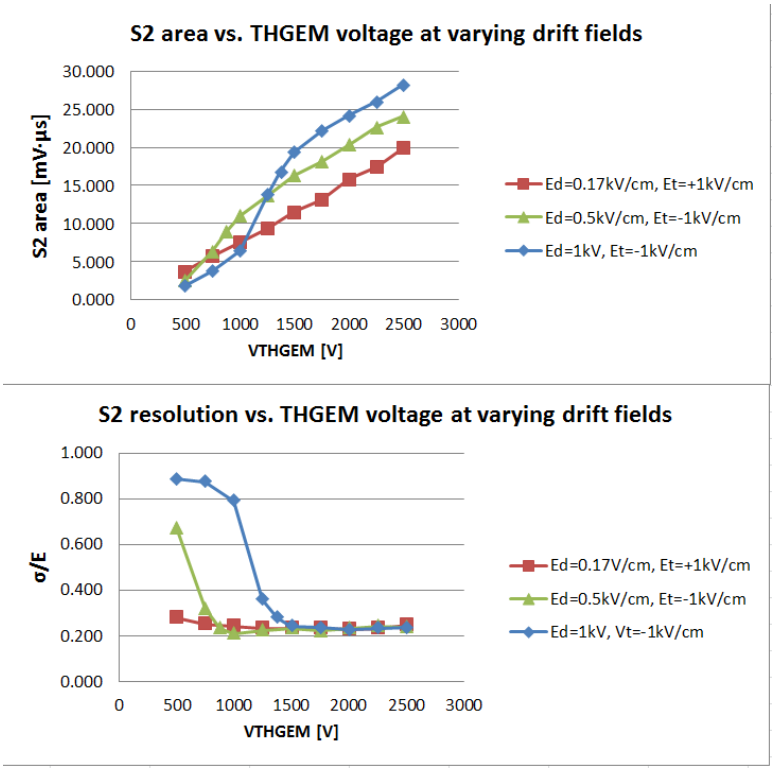

Figure 24 S2 area and resolution as a function of the THGEM voltage with varying drift fields. The "knee" structure which increases with drift field seen on the left plot corresponds to the transition from partial to full focusing of electrons into the holes. The same effect is manifested in the resolution of the pulses when less collection of electrons yield a wider spread of the signal. At high enough THGEM voltage, larger S2 with growing drift field corresponds to a larger fraction of electrons escaping recombination.

3.3 "*Super-Stable*" conditions

The accidental discovery of the super-stable conditions, mentioned above and seen clearly in Figure 16, caught us for its first appearance unprepared. In order to reestablish these conditions we decided to cool down the cryostat back to 163K and repeat the process above. This time however, intending to acquire waveforms of S1 and S2 while in stable conditions and during constant monitoring of the rate. The acquisition setup is the same as depicted in Figure 15. The temperature of the fins was then raised by 10 degrees to 173K. A first trial (the trigger rate is shown in Figure 25) was unsuccessful, after ~13.5 hours S2 reappeared though unstable as in normal operation. A second attempt was done afterwards, the temperature was raised by one degree (from 173K to 174K) and, after one hour of no S2 triggers, S2 appeared super-stable (without fluctuations in the counting rate of S2). These conditions were maintained for ~1.5 hours during which S2 waveforms were continuously recorded. The reasons for the appearance or lack of appearance of the stable conditions after a step increase in pressure are not yet clear to us and will require further investigations in the future.

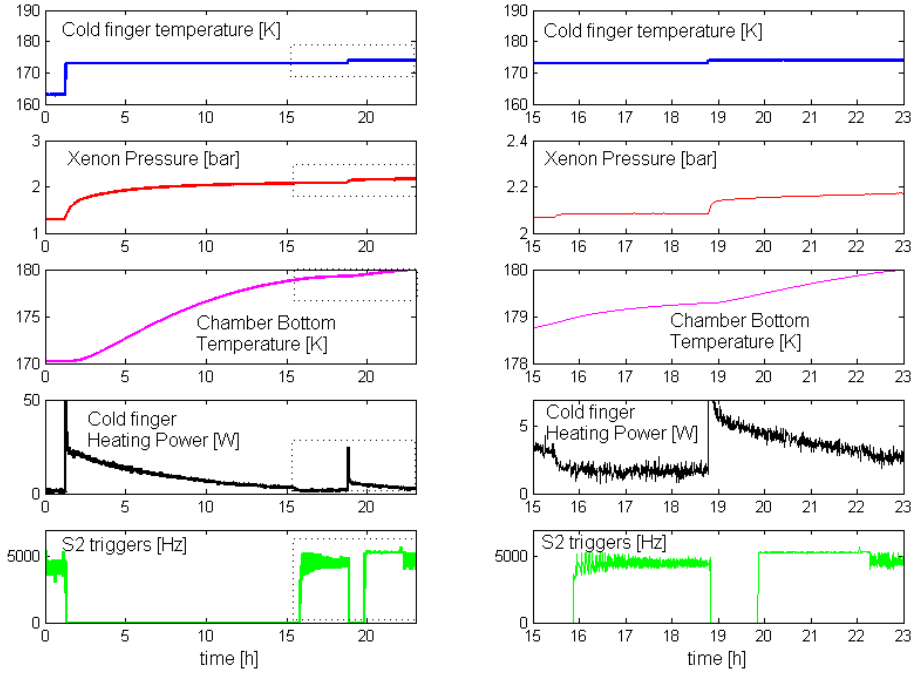

Figure 25 Disappearance and reappearance of S2 signal after a step increase in pressure. After the first increase, the S2 signal appeared unstable, as in normal running conditions. A further increase of 1 degree in the fins' temperature resulted in the reappearance of the super stable S2 regime.

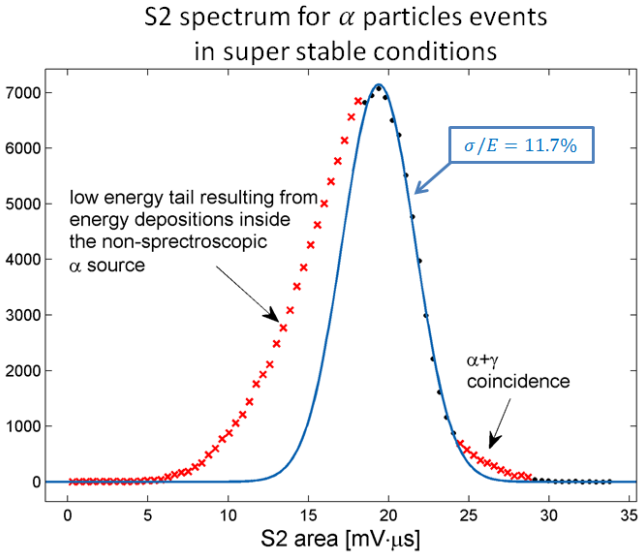

Figure 26 S2 spectrum in super stable conditions. Post processing included cuts on S1 area to avoid59.5 keV gamma induced events. Double-peak S2 and long rise-time S2 pulses have also been discarded to avoid the coincidence of α and γ. Still, as explained above, some events do not fall into these catagories, and leave a feature to the right of the main peak, as marked on the figure. The resolution deduced from a Gaussian fit to the right hand side of the peak is 11.7% - well below the numbers presented before for normal operation (~20%).

The recorded waveforms were taken for post processing. Cuts applied to these included the requirement for alpha particle emission at close to 90° to the source surface (namely, demanding that $S1 > 0.1\,mV \cdot \mu$ sec), as described earlier. Further cuts aimed at discarding the coincidence of the alpha and gamma events were applied as well. A spectrum of the alpha-induced S2 electroluminescence signals is shown in Figure 26. A Gaussian fit performed on the right hand side of the peak shows a very good resolution of $11.7\%\ \sigma/E$

compared to the non-stable regime where a resolution of ~20% σ/E was obtained. For comparison, the XENON100 reported a S2 resolution of 15% for 60 keV gammas [12]). A slight "tail" can also be seen, of higher pulse-heights. This is attributed to coincidence events which were not discarded based on pulse-shape cuts. The left hand side of the spectrum shows the broadening due to energy deposition of the alpha particles in the source matrix.

3.4 S1 variations with THGEM voltage

During all measurements, both at stable conditions with constant S2 and after a step increase in pressure where S2 disappears, waveforms and spectra of S1 scintillation were also recorded. Analysis of the spectra uncovered a surprising behavior in the different regimes (see Figure 28). During the transient following a step increase in the pressure, when the system was at 2.3 bar with no S2 (and supposedly no vapor under the THGEM), a change in the THGEM voltage had no effect on the mean value of the S1 distribution. However, as soon as the thermodynamic conditions stabilized and S2 reappeared, a reduction of the S1 signal by a factor of ~2 was observed. We attribute this reduction to total internal reflectance of S1 photons from the interface between the bubble sitting in the THGEM hole and the liquid above it. To that end, the curvature of the liquid-gas interface is important. An S1 photon emitted from the alpha particle track, which reaches the THGEM plane at an incidence angle small enough to pass through the THGEM hole towards the PMT would be, nearly always, below the critical angle for total internal reflectance from a hypothetical planar liquid-gas bubble interface[3]. Only a curved liquid gas interface (e.g. as shown in Figure 27) would explain total internal reflection that reduces the number of photons hitting the PMT.

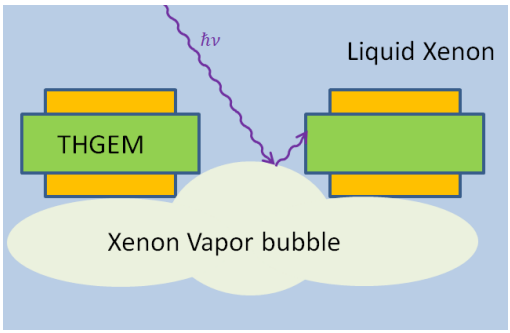

Figure 27 A proposed scenario of full internal reflection of a photon from the liquid vapor interface at a bubble located under a THGEM hole.

3 The maximum incidence angle that a photon can have, relative to the THGEM surface, and still be able to pass through the hole, is dictated by the ratio between the hole diameter and FR4 thickness. For the THGEM used in this work the hole diameter is 0.3 mm and FR4 thickness is 0.4 mm, so that the maximum incidence angle is $\tan^{-1}(0.3/0.4) = 36.9°$. The critical angle for total internal reflection at an interface between LXe and xenon gas depends on the refractive index of LXe at 178 nm. Values in the literature vary from n=1.54 to n=1.69 (See [10] [52] [53] [54]), corresponding to a critical angle between 36.3° and 40.5°.

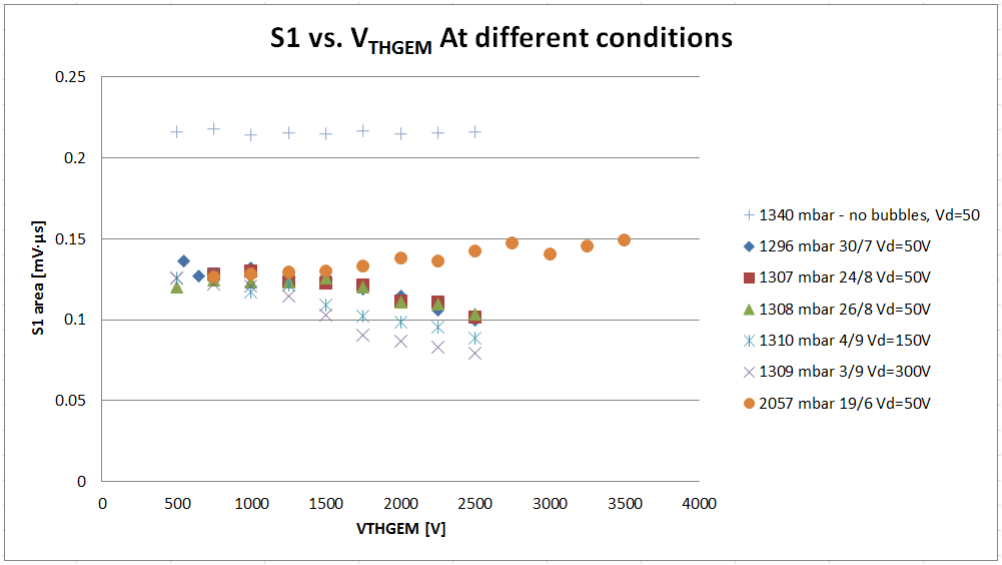

Figure 28 S1 variations with THGEM voltage at different thermodynamic conditions and different voltages. S1 is reduced by a factor of ~2 when bubbles appear under the THGEM surface. Interaction of the electric field gradients with dipoles induced in the liquid change the form of the liquid-vapor interface, affecting total internal reflection.

Moreover, as seen in Figure 28 we note that a change in the THGEM voltage results in a change of the S1 average intensity; the phenomenon is pressure dependent. We attribute that, though further simulations and experimental proof is needed, to the effect of electrostriction [48] (suggested also in [49]). Namely, dipoles in the dielectric liquid induced by the strong electric field inside the holes interact with gradients of the electric field, creating a pressure field in the liquid. The electrostriction force is of the same order of magnitude as the other relevant forces (pressure, surface tension). This would result in a deformation of the bubble shape, leading to a change of the total-internally-reflecting surface, and consequentially to a change in the intensity of light passing through it.

3.5 Estimates of vapor layer thickness

The electroluminescence occurring in the gas phase only can serve as a probe for the location and thickness of the vapor bubbles in the liquid volume. Introducing a high transfer field resulted in a change of the S2 waveform shape as seen in Figure 29. With growing transfer field, there is a gradual widening of the pulse-shape that reaches saturation at $1\ \mu s$. With low transfer field, electrons induce electroluminescence only in the high field region in the hole until eventually reaching the bottom THGEM electrode (for very low and for negative transfer fields, see Figure 23) or the low field region of the transfer gap (for slightly higher transfer field values). At high fields however electrons induce luminescence along their entire trajectory in the gas. The width added to the pulse shape hints that electrons travel a distance in the gas of $\sim 1\ mm$ (derived from the drift velocity of electrons in GXe [50]) which consequentially hints on the typical size of the bubble. When a drift field up to $11\ kV/cm$ was applied over the drift gap (setup of Figure 7), no apparent luminescence was observed, suggesting that there are no bubbles in the drift volume.

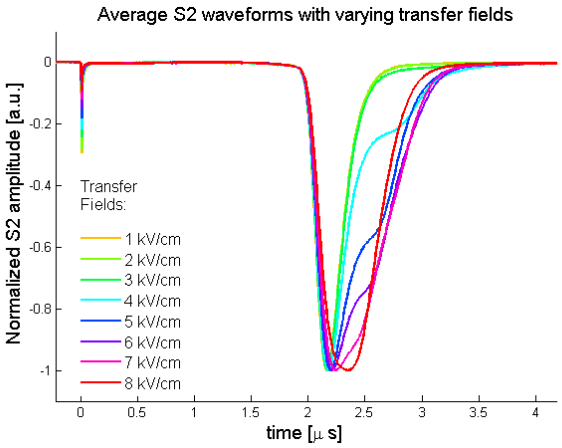

Figure 29 S2 waveform at different transfer fields. The widening of the waveform hints on the size of the bubble underneath the THGEM.

4. Results in MiniX

4.1 First liquefaction

The first successful liquefaction of xenon in MiniX took place on December 15th; it resulted in 0.5 liters of liquid xenon in the cryostat. Cooling down to liquid xenon temperature took ~2 hours and complete filling of xenon took an additional hour. A temperature of $\sim 170K$ could not be kept using only the $50\,W$ from a single $50\,\Omega$ resistor, due to the large heat conductivity of the copper rod (see Figure 10). Additional power ($12.5\,W$) was added, using the second heater at the bottom of the inner copper cup, enabling the stabilization of the temperature. Adding the additional power however results in a quicker evaporation of the LN_2, forcing a too-frequent replacement of the LN_2 supply dewar (and is costly). A more elegant solution would be the introduction of insulation between copper rod and inner cup (e.g. using a stainless steel disc). The drawback of this is a longer initial cool-down and liquefaction time.

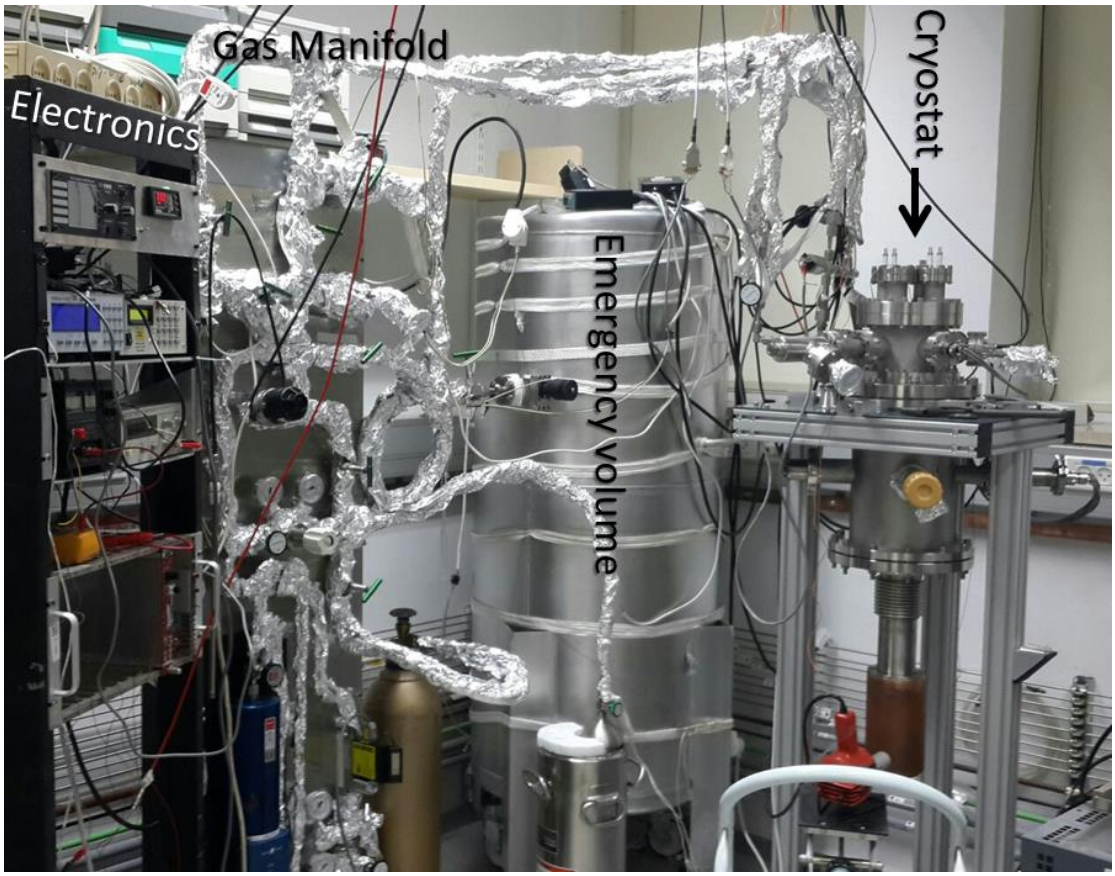

Figure 30 MiniX cryostat, the gas manifold, the emergency volume and electronics in the laboratory.

The total heat flux dissipated in the LN_2 was calculated using the temperature gradient on the copper rod according to $\dot{Q} = C \cdot \Delta T \cdot A/L$, where C is the heat conductance of the copper , ΔT is the temperature difference at its ends and A and L are the cross-section and the length of the rod. Introducing the numbers reads $\dot{Q} = 400\frac{W}{m \cdot K} \cdot (167K - 77K) \cdot$

$\frac{\pi \cdot (17.5mm)^2}{465\ mm} = 74W$. Liquid xenon was kept in the cryostat for two days during which the cryogenics infrastructure systems (temperature control and LN_2 automatic filling system) showed flawless operation.

Circulating the liquid through the purification system as described above introduces a heat load on the cryostat. The heat exchanger efficiency can then be calculated. Taking into account the xenon latent heat and the specific heat of xenon gas, $1\ slpm$ (standard liter per minute) of xenon evaporated, heated to room temperature and re-liquefied results in a heat load of $9.6\,W$. Since the system is under a constant control loop for temperature stabilization, the actual extra heat load can be read form the drop in the heating-resistor's power. At the transition from $1\ slpm$ to $1.5\ slpm$ the heat load changed by $4.5W$ suggesting a rather poor heat transfer efficiency of $\sim 7\%$ at the quoted flow. At flow values relevant to the system ($1-2\ slpm$), this results in an increase of $9-18\,W$ in heat load. As the introduction of a longer or an external heat exchanger requires a more complex design, the extra heat load is tolerable.

Stable and accurate control over the thermodynamics of the system was not yet achieved during liquid circulation at the time of writing this work. The pressure in the vessel increases to a value larger than the liquid-vapor equilibrium pressure as soon as circulation starts. Moreover, the pressure seems to fluctuate within 10%, with a time scale of tens of seconds, around its mean value. Similarly, fluctuations are seen also in the reading of the mass flow controller (order of 50% at a time scale of seconds).

The source of these fluctuations are not yet clear to us. They could be due to liquid boiling in the outlet line, causing pressure bursts in the pump and in the flow controller which is then unable to stabilize the gas flow. A possible solution could be the introduction of a buffer volume before and after the pump to damp these fluctuations. A second potential source for thermodynamic instability could originate from the liquid level in the LXe chamber reaching the height of the liquefaction ring. A partial coverage of the coldest wall area might reduce the cooling power, thus causing pressure fluctuations. Avoiding this scenario could be done by keeping the liquid level constantly beneath the liquefaction ring or by replacing the liquid volume container with a copper wall to make the temperature field more uniform.

4.2 Generation of bubbles on thin resistive wires

For the first liquefaction studies in MiniX, a setup was assembled including a resistive-wire electrode, located above the mesh electrode and the bottom PMT, as shown in Figure 31. The resistive wire array was introduced to perform a qualitative study of bubble formation when heated. The $55\mu m$ thick resistive $NiFe$ wire was wound with 4mm pitch (total resistance of $62.5\,\Omega$ at a length of $\sim 28\,cm$), on a G10-made circular frame; it was sandwiched between two G10 holders above the bottom mesh (schematics in Figure 31, picture from top window in Figure 32). The detector assembly was removed in this study; a window was assembled on one of the four CF ports of the top flange. A 50mm focal length Canon lens was placed above the window, followed by a webcam CCD sensor, to film the creation of bubbles on the wires. The illumination was done with a LED from the top flange.

Due to the large distance between the wires and the viewport, accurate observations could not be made. Still, one could observe three different regimes induced by the current passing through the wire. At low currents ($0 - \sim 200\ mA$), there seem to be only convection around the wire but no evidence for vapor. At higher current values ($\sim 200 - \sim 300\ mA$), a shiny layer appeared around the wire (see Figure 32C); it could be attributed either to a vapor layer encompassing it or to reflection or refraction due to local changes in the refraction index. The third regime ($\sim 200 - \sim 300\ mA$) occurred when large bubble were formed on the wires and detached from them at a high rate – causing the liquid to boil (in this regime, the wires were not visible anymore). The onset of the different regimes is not a step function, but rather a smooth behavior. The system shows hysteresis effects as well, as the onset value of a regime is different than the return to previous regime. The boiling regime started around $\sim 300\ mA$; it is in agreement with the power density of $1 - 2\ W/cm$ needed for boiling LXe, suggested in [49].

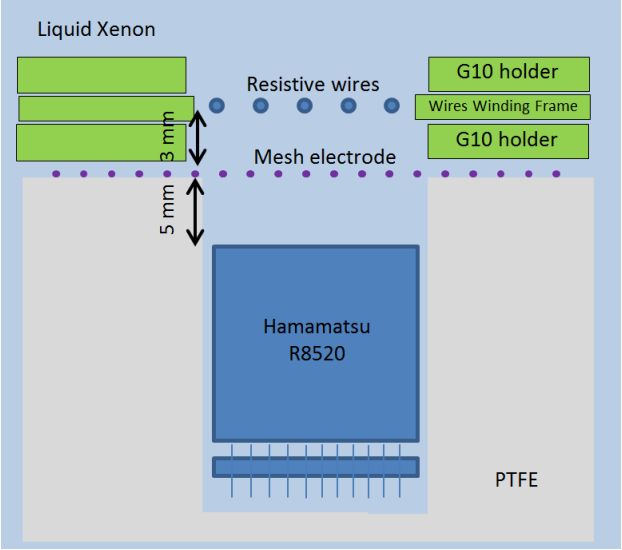

Figure 31 MiniX setup for the first liquefaction. Heating wires for the study of bubble formation were immersed in liquid xenon. Current was passed through them to study the boiling of the xenon. Optical recording of the bubbles was done via a 2.75'' CF viewport on the upper most flange (not shown).

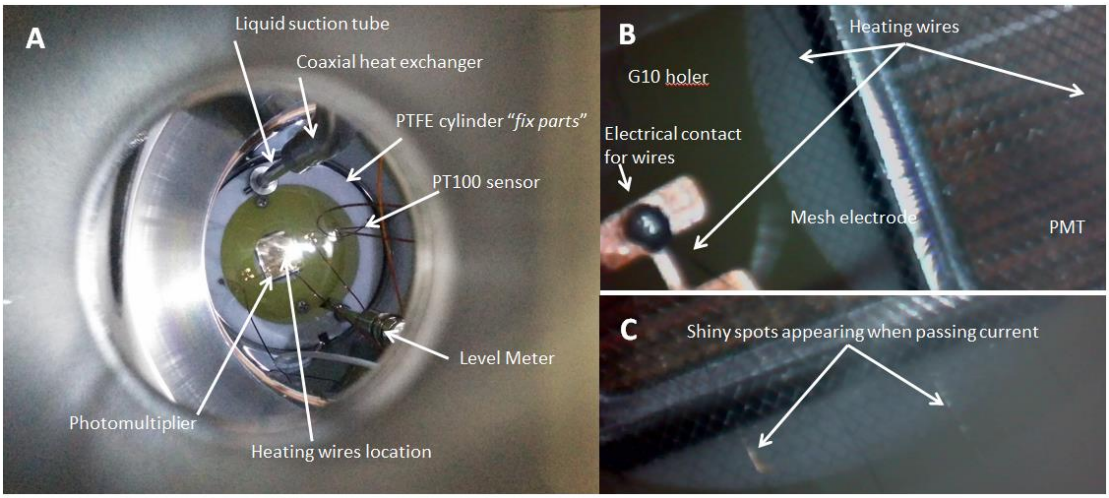

Figure 32 (A) Picture taken from the top flange's window (using a cellphone camera) looking at the setup of the first liquefaction. The *Fixed-parts* bottom PTFE block can be seen with its Pt100 sensor, level meter, PMT, liquid suction tube as well as part of the coaxial heat exchanger. (B) Picture taken with the 50mm Canon lens and a webcam CCD sensor. Heating wires as well as the mesh electrode, the PMT, the electrical contacts for wires and the G10 holders are seen. (C) At moderate currents ($\sim 200 - \sim 300\ mA$), shiny spots along the wire begin to appear corresponding to either a thin layer of vapor around them or to diffraction due to local changes in density.

4.3 LHM element with resistive wires for bubbles creation

Following our assumption that light is created in the THGEM holes only in the presence of a vapor layer/bubble underneath it, we have decided to build a simple setup to demonstrate this. The new setup, including the resistive wires frame, was mounted as the *detector assembly* suspended from the top flange. A THGEM was placed inside the liquid with an ^{241}Am source $4mm$ above it; the resistive wires (same as described above) were placed $6mm$ underneath. A PMT was assembled above the source facing down, recording S1 reflected photons and serving as a trigger. S2 signals were recorded on the bottom PMT. The setup is schematically shown in Figure 33.

With no current applied to the wires, the application of voltages (-1600 V on source, -1300 V on THGEM top, -300 V on THGEM bottom and zero voltage on the wires) did not show any S2 signal. However, when the current on the wire reached $\sim 280\ mA$ S2 signals started appearing. A picture showing both the current through the wire and the oscilloscope showing both S1 and existent/nonexistent S2 signal is shown in Figure 34). Turning off the heating current abruptly did not suppress S2 signals immediately; this is expected, as it takes some time to the bubbles to collapse. Reducing the current on the wire to levels slightly below the threshold for S2 appearance did not suppress S2. This indicated upon some hysteresis process which should be better understood once the G-MiniX setup is functional.

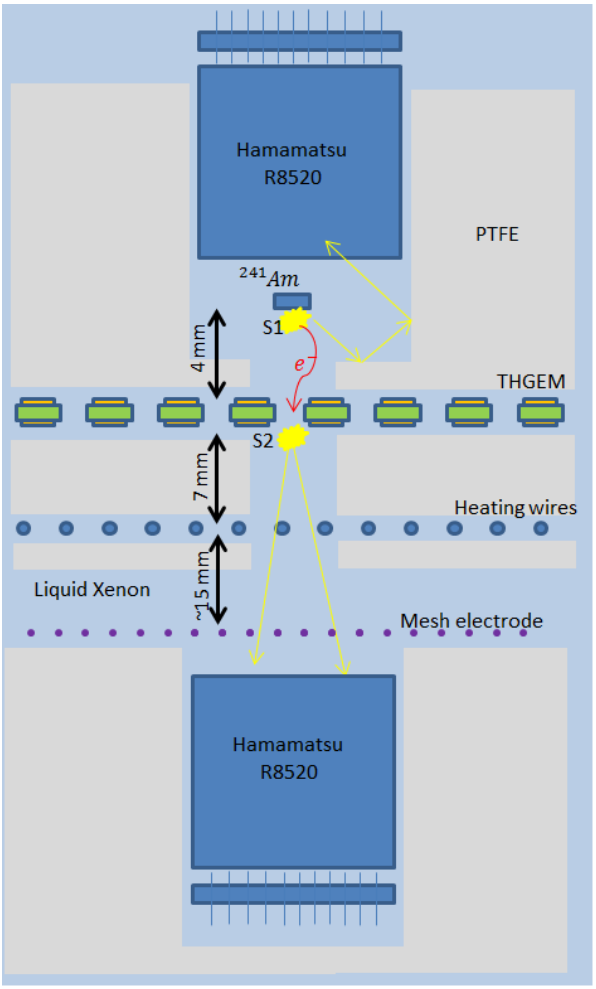

Figure 33 LHM/resistive-wires setup in MiniX. An americium source emits alpha particles into the liquid. Prompt scintillation light is recorded both on the top PMT via photons reflected off the PTFE walls. Ionization electrons drift towards the THGEM where they induce electroluminescence - only upon the supply of a sufficiently intense current to the heating wires, for the creation of bubbles. Electroluminescence photons are mainly recorded on the bottom PMT.

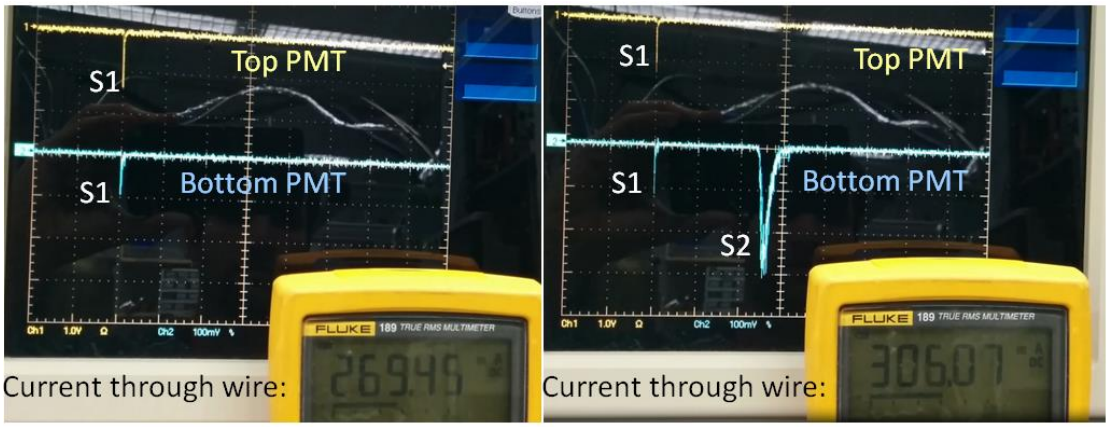

Figure 34 Oscilloscope and multimeter screenshots showing the top and bottom PMT signals and the current through the heating wire. Left: heating current (269 mA) of the wire below threshold for S2 appearance – only S1 is seen on both PMTs. Right: higher current (306mA) caused bubbles to form, and accumulate underneath the THGEM electrode - inducing S2 electroluminescence. The latter is seen as large S2 pulse recorded on the bottom PMT.

4.4 Charge Collection

As described above, the control over the stability of the thermodynamics in circulation mode is at the moment somewhat problematic. Measurements of bubble creation and disappearance, and especially the onset of the bubbles and S2 appearance requires stable thermodynamic conditions. Stopping circulation means a potential gradual degradation of the purity of the liquid. The latter is usually measured in terms of the lifetime of electrons drifting under an electric field before attachment to electronegative impurities [10] which removes them from the measureable charge signal. We have thus initiated a study to understand the effects induced by stopping the gas circulation on the purity of the liquid; the hope is to be able to conduct measurements on relatively short time scales - without circulation.

The measurements were conducted in the setup of the LHM with wires underneath, shown in Figure 33. All electrodes except the source were grounded. A charge-sensitive preamplifier (Canberra 2006) was connected to the top THGEM electrode (grounded via a $110\ M\Omega$ resistor). The signal was then processed by a linear amplifier (Ortec 572A) at a gain of 1000 and $2\ \mu s$ shaping time. Due to the poor signal-to-noise conditions, a trigger from the bottom PMT was employed. The setup is schematically shown in Figure 35. The charge integration chain was calibrated using $50mV$ square pulses injected to the test input of the preamplifier. Examples of waveforms can be seen in Figure 36.

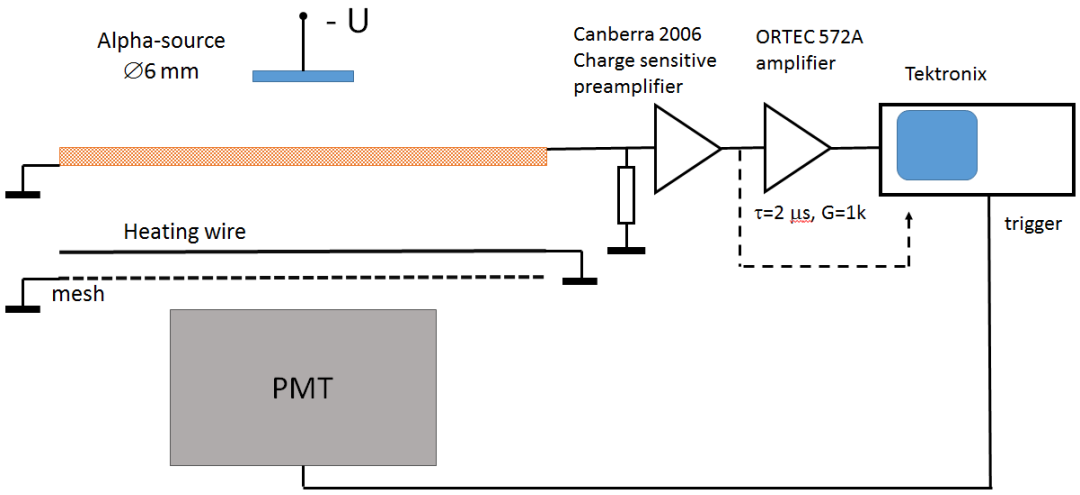

Figure 35 Schematics of the setup for charge collection measurements. Charge is collected on top THGEM electrode, transferred to a charge sensitive preamplifier, to a linear amplifier and to an oscilloscope. The trigger is supplied by the bottom PMT.

The measurements were performed after the condensation of ~1/4 of the amount of xenon in the vessel, while the other 3/4 was not circulated for a few hours before measurements. As the noise was high, averaging of the waveforms was necessary to eliminate random pickup noise. All measurements were corrected for an offset value measured as the charge collected at zero electric field. The charge as a function of the electric field, as well as a comparison to [51] is seen in Figure 36.

The charge collected here is a factor of two less than the charge published in [51], this might be due to the impurity level of the system (leading to charge loss during drift). However, despite considerable efforts by colleagues[4], the values published in [51] remain the highest ever published and, as far as we know, have never been obtained again. Whether the absolute charge we measure is low due to impurities or not remains therefore unresolved. However for practical purposes, this charge collection will suffice for the prospected near-future studies.

The charge collected was measured as a function of time (Figure 37) after the start of circulation and after an increase of the flow. A slight improvement in charge collection can be seen over time. However, the time scale of the purification of the liquid is different than that of its contamination: the former is dominated by the recirculation flow, while the latter – by the release rate of impurities from inner surfaces. Therefore, in order to draw definite conclusions regarding the "safe period" (the time the system can run with no circulation without being significantly contaminated), a measurement of charge collection following the stop of recirculation is still required. Such a measurement would also benefit from a reduction of noise level (by carefully shielding the cables and improving the groundings of the system).

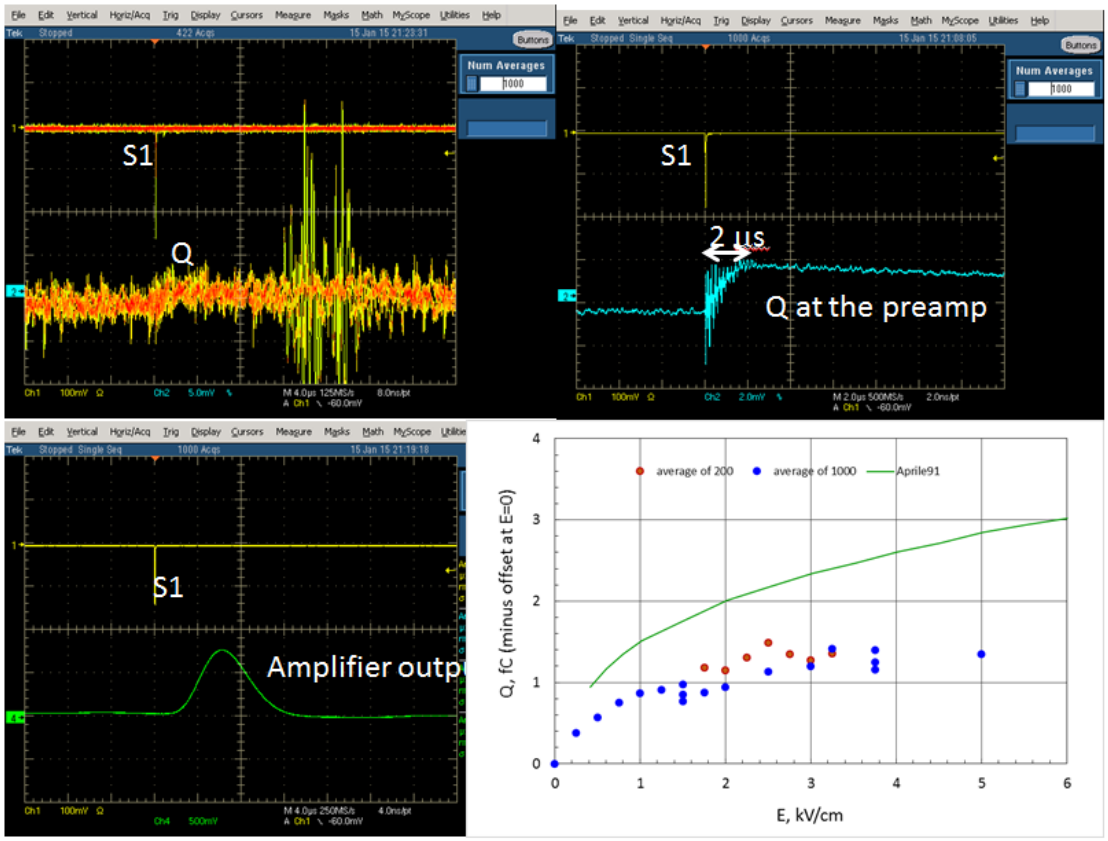

Figure 36 Top left: charge pulses from the preamplifier on oscilloscope (persistence mode). Top right: charge signal from preamplifier, averaged over 1000 waveforms. Bottom Left: linear amplifier output averaged over 1000 waveforms. Bottom right: charge collection corrected for offset and compared to [51].

[4] V. Chepel, Private communication.

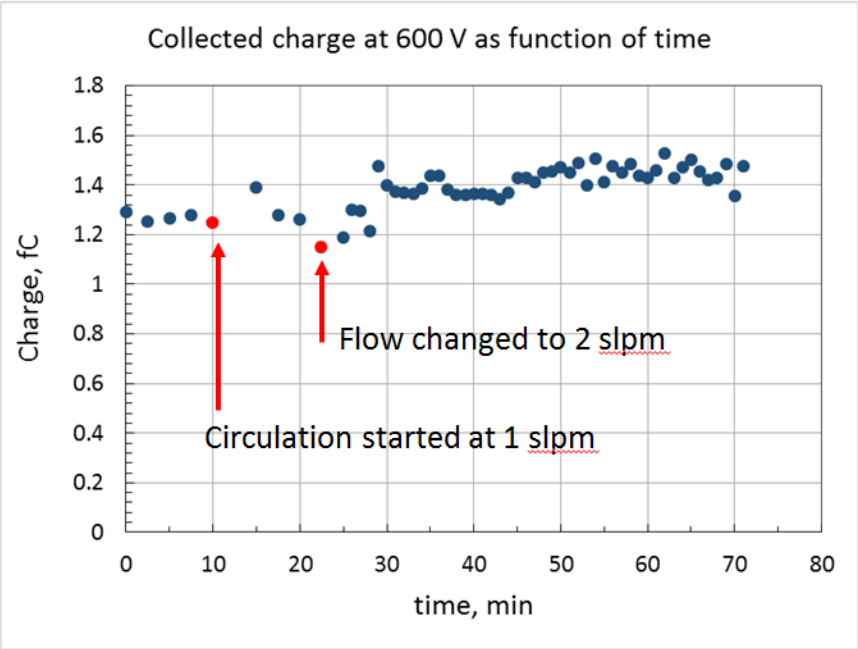

Figure 37 Charge collection as a function of time when circulation starts at 1 slpm and at when raised to 2 slpm. A slight improvement in charge collection is seen ~30 minutes after flow raised to 2 slpm.

5. Discussion and future plans

In this work, we demonstrated the principle of a *bubble-assisted LHM* mechanism – a "local dual phase" scheme, with proportional electroluminescence occurring within gas bubbles trapped under a THGEM electrode immersed in liquid xenon. We have shown that under thermodynamic conditions allowing for bubbles to form, the electroluminescence caused by radiation-induced electrons drifting into the electrode's holes was relatively stable and reproducible over a period of few months. We have shown that during transients following an increase in the system's pressure, the bubbles collapse - thus causing the electroluminescence signal to disappear. Under steady-state boiling conditions, we have investigated the dependence of the electroluminescence yield and resolution on the physical parameters (voltage across the electrodes, drift and transfer fields as well as the pressure). At normal stable operation, the detector reached an RMS energy resolution, for alpha particles of ^{241}Am, as low as $\sigma/E \sim 20\%$. Bearing in mind that under steady state operation the signal's resolution is widened also due to slow modulations (with period of few seconds) in the mean of the signal, one could assume that more stable operation conditions exist. Indeed, shortly after the transition from a non-boiling to a boiling state, we have shown the existence of a "*super-stable*" regime, during which, for a short period of time, the detector has shown a surprisingly good resolution - $\sigma/E \sim 12\%$.

The promising preliminary results, with an energy resolution comparable to the S2 resolution of the XENON100 experiment, call for additional, more systematic studies, towards a potential application of the LHM concept for future DM experiments. At present, one could conceive a *single phase* TPC with LHM elements (assuming an adequate and controllable bubbles creation mechanism) as WIMP-induced scintillation (S1) and electroluminescence (S2) detectors within the liquid, as shown in Figure 38. Additional photon detectors (such as gaseous photo multipliers) could cover the walls and the top of the detector allowing for a full 4π coverage of photons detectors. Such a detector may potentially overcome the difficulties associated with the construction of a large volume 'classic' dual-phase TPC detectors, while keeping its advantages (combined light and charge measurement).

Still, there is a long way to go. The indirect evidence for bubble formation and their subsequent trapping under the THGEM, shown here, may be convincing, but a final proof would be their direct observation. Furthermore, many questions regarding the interpretation of our data have been left unanswered. Among them are: where do the bubbles form? What is their actual size? Do the bubbles remain underneath the entire THGEM-electrode surface or just under the holes? Are they constantly formed? If so, where do they go? A study intended for a well-controlled formation of the bubbles or gas layer under the hole-electrodes is the key to the successful development of a "*bubble-assisted LHM*" detector.

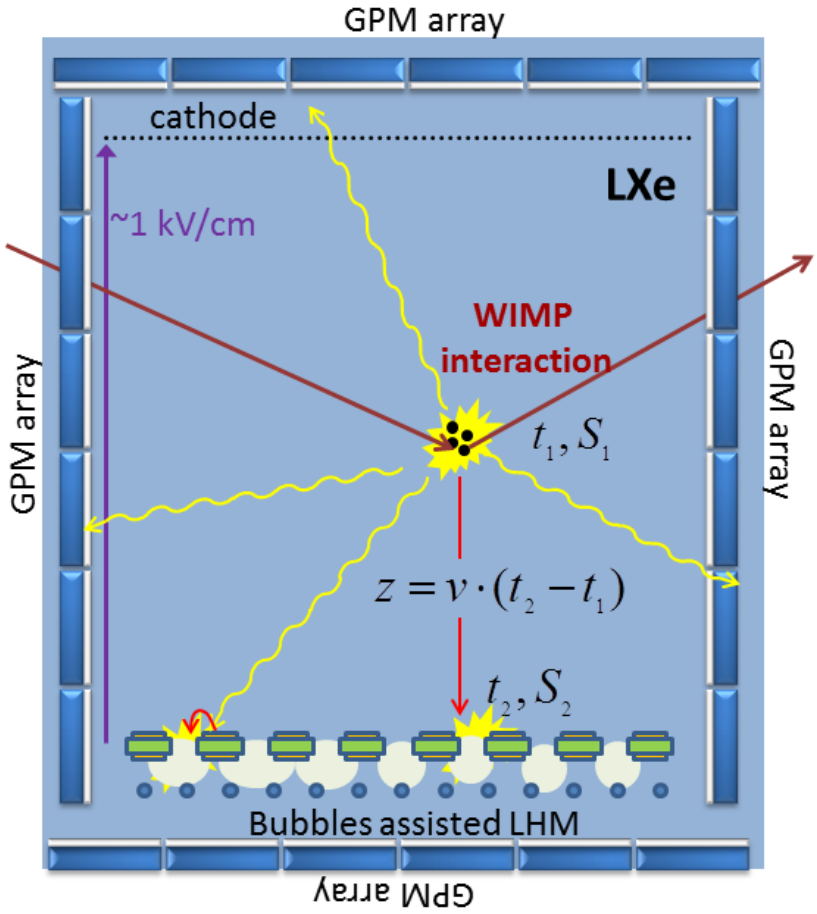

Figure 38 A schematic design of a TPC detector with a LHM element at the bottom. The LHM operates in a bubbles-assisted electroluminescence mode, where here the bubbles are created by heating wires. Prompt scintillation (S1) photons are recorded on the top array of photon detectors (GPM), on the surrounding walls GPM arrays and on the CsI-coated LHM element (bottom). Electrons drift downwards to the LHM detector, enabling the detection of the secondary signal, recorded eventually by an array of GPM located under the LHM element. Position reconstruction, energy reconstruction and discrimination of nuclear recoils and electronic recoils are done similarly to the current technique in dual-phase detectors.

The MiniX cryostat was designed and built for this purpose; it is an ideal playground for future studies. With the G-MiniX setup (now under final stages of production), it is suggested to focus on the mechanism of liquid-xenon boiling and trapping of the resulting bubbles underneath the THGEM electrode. The system, cooled by liquid nitrogen, permits similar investigations in liquid argon. Different methods of bubble creation should be considered, e.g. passing current through a heating surface, through resistive wires or even by replacing the bottom THGEM copper electrode by a resistive surface. The properties of the heating and bubbling mechanism should be adapted to eventually reconstruct conditions similar to that of the "super-stable" ones demonstrated above in WILiX. The success of building a "local-dual phase" TPC, of a design similar to that in Figure 38, with robust control, guaranteeing continuous operation in such super-stable conditions, may pave the way to solving potential problems foreseen when scaling-up future dark matter detectors.

In parallel to the study of bubble formation in THGEM electrodes, it is suggested to investigate the LHM with a GEM (Gas Electron Multiplier) element. GEMs, due to their ten-

fold thinner geometry, allow the creation of larger fields inside their ~50 micrometer diameter holes. Such fields are potentially sufficient for inducing electroluminescence *in the liquid itself*. With electroluminescence in the liquid, a *single phase* TPC-detector configuration with additional vertically situated LHM elements could become possible. This in turn will allow also for wall coverage with sensors, with the possibility of enhancing S1 detection efficiency for lower-mass WIMPs. Also, as suggested in Figure 39 a 4π coverage with LHM elements will enable splitting the detector into two parts, thus lowering the drift voltages - facilitating the design of large-volume detectors.

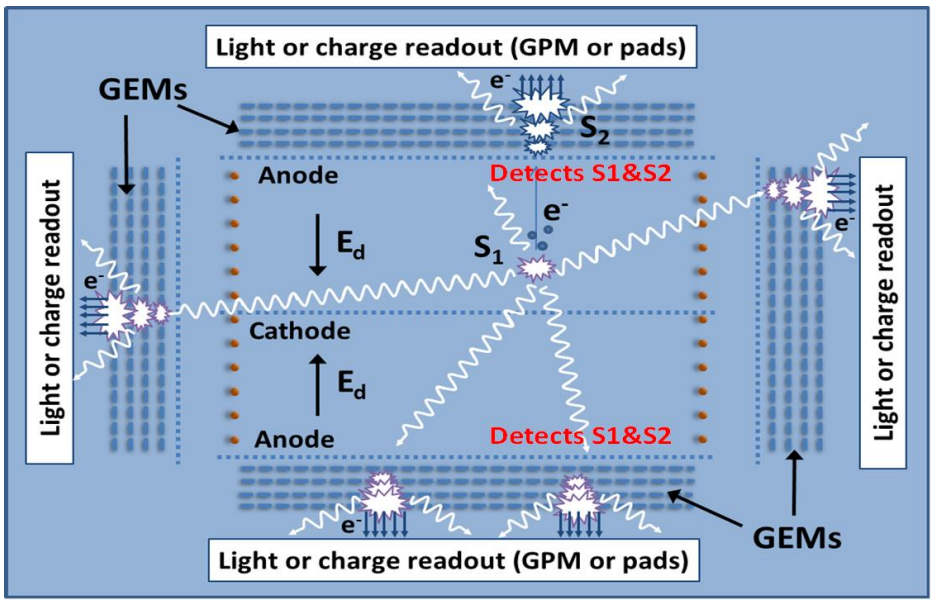

Figure 39 Assuming a GEM can create fields high enough for the electroluminescence in liquid, one could conceive a single phase TPC with LHM elements, of a 4π S1 detection coverage. A cathode in the middle of the cryostat, splitting the volume into two drift regions, allows application of lower voltages than a single drift. With permission from [23].

6. Bibliography

[1] Planck Collaboration: P. A. R. Ade et al., *Planck 2013 results. XVI. Cosmological parameters,* arXiv:1303.5076.

[2] G. Bertone, D. Hopper, J. Silk, "Particle dark matter: evidence, candidates and constraints," *Phys. Rept.,* vol. 405, no. 5-6, pp. 297-390, 2005.

[3] G. Jungman, M. Kamoinkowski, K. Griest, "Suppersymmetric dark matter," *Phys. Rept. ,* vol. 267, pp. 195-373, 1996.

[4] P. Cushman, C. Galbiati, D. N. McKinsey, H. Robertson, T. M. P. Tait et al., "Snowmass CF1 Summary: WIMP Dark Matter Direct Detection," *arXiv:1310.8327,* 2013.

[5] XENON100 collaboration: E. Aprile et al., "Dark Matter Results from 225 Live Days of XENON100 Data," *PRL,* Vols. 108, 181301, 2012.

[6] LUX collaboration: D.S. Akerib et al., "First results from the LUX dark matter experiment at the Stanford Underground Facility," *PRL,* Vols. 112, 091303, 2014.

[7] L. Baudis, "Direct dark matter detection: the next decade," *Phys. Dark Universe,* vol. 1, pp. 19-108, 2012.

[8] CDMS Collaboration, "Silicon Detector Dark Matter Results from the Final Exposure of CDMS II," *PRL,* Vols. 111, 251301, 2013.

[9] D. Akimov, "Techniques and results for the direct detection of dark matter (review)," *Nucl. Instum. and Meth.,* vol. 628, pp. 50-58, 2011.

[10] E. Aprile and T. Doke, "Liquid xenon detectors for particle physics and astrophysics," *Rev. Mod. Phys. 82,* pp. 2053-2097, 2010.

[11] V. Chepel and H. Araujo, "Liquid noble gas detectors for low energy particle physics," *JINST,* vol. 8 R04001, 2013.

[12] E. Aprile, K Arisaka, F Arneodo, A Askin, L Baudis, A Behrens et al., "The Xenon100 experiment," *Astroparticle Physics,* vol. 35, no. 9, pp. 573-590, 2012.

[13] X. G. Cao et al., "PandaX: A Liquid Xenon Dark Matter Experiment at CJPL," *Sci China-Phys. Mech. Astron.,* vol. 57, pp. 1476-1494, 2014.

[14] D .S.Akerib et al., "The Large Underground Xenon (LUX) Experiment," *Nucl. Instum. Metho.,* vol. A704, pp. 111-126, 2012.

[15] T. Alexander et al., "DarkSide search for dark matter," *JINST,* vol. 8, p. C11012, 2013.

[16] E. Aprile (for the XENON1T collaboration), "The XENON1T Dark Matter Search Experiment," *Springer Proc. Phys.,* vol. 148, pp. 93-96, 2013.

[17] C. Amsler, A. Badertscher, V.Boccone, A.Bueno, M.C.Carmona-Benitez, W.Creus et al., "First results on light readout from the 1-ton ArDM liquid argon detector for dark matter searches," *JINST,* vol. 8 P11003, 2010.

[18] A. Hitachi, T. Doke, and A. Mozumder, "Luminescence quenching in liquid argon under charged-particle impact: Relative scintillation yield at different linear energy transfers," *Phys. Rev. B,* vol. 27, no. 9, pp. 5279--5285, 1983.

[19] L. Baudis (for the DARWIN consortium), "DARWIN dark matter WIMP seatch with noble liquids," in *J. Phys.: Conf. Set. 375 012028; arXiv: 1201.2402v1*.

[20] E. Aprile, P. Cushman, K. Ni,, "Detection of liquid xenon scintillation light with a silicon photomultiplier," *Nucl. Inst. and Meth.,* vol. 556, no. 1, pp. 215-218, 2006.

[21] L. Arazi, A. E. C Coimbra, I. Israelashvili, E. Erdal, M. L. Rappaport, D. Vartsky and A. Breskin, "Advances in cryogenic gaseous photomultipliers for future noble-liquid detectors for dark matter and rare event searches," *In preparation.*

[22] V. Boccone et al., "Development of wavelength shifter coated reflectors for the ArDM argon dark matter detectors," *JINST,* vol. 4 P06001, 2009.

[23] A. Breskin, "Liquid Hole-Multipliers: A potential concept for large single-phase noble-liquid TPCs of rare events," *J. Phys. Conf. Ser. 460 012020,* 2013.

[24] E. Aprile, A. Bolotnikov, D. Chen, R. Mukherjee, F. Xu, D.F. Anderson, V. Peskov., "Performance of CsI photocathodes in liquid Xe, Kr, and Ar," *Nucl. Instrum. Meth. A,* vol. 338, pp. 328-335, 1994.

[25] A. Breskin, R. Alon, M. Cortesi, R. Chechik, J. Miyamoto, V. Dangendorf, J. Maja, J.M.F. Dos Santos, "A concise review on THGEM detectors," *Nucl. Instr. Meth. A598,* pp. 107-111, 2009.

[26] F. Sauli, "GEM: A new concept for electron amplification in gas detectors," *Nucl. Instr. and Meth.,* vol. A386, p. 531, 1997.

[27] M. Cortesi et al., "Concept of a novel fast neutron imaging detector based on THGEM for fan-beam tomography applications," *JINST,* vol. 7 C02056, 2012.

[28] A. Breskin et al., "CsI-THGEM gaseous photomultipliers for RICH and noble-liquid detectors," *Nucl. Instum. and Meth.,* vol. 639, no. A, pp. 117-120, 2011.

[29] M. Alexeev et al., "Development of THGEM-based Photon Detectors for COMPASS RICH-1," *Physics Procedia,* vol. 37, p. 781–788, 2012.

[30] S. Duval et al., "Hybrid multi micropattern gaseous photomultiplier for detection of liquid-xenon scintillation," *Nucl. Instum. and Meth.,* vol. 695, p. 163–167, 2012.

[31] S. Duval et al., "On the operation of a micropattern gaseous UV-photomultiplier in liquid-Xenon," *JINST,* vol. 6 P04007, 2011.

[32] K.L. Giboni, X. Ji, H. Lin and T. Ye, "On dark matter detector concepts with large-area cryogenic Gaseous Photo Multipliers," *JINST,* vol. 9, p. C02021, 2014.

[33] E. Aprile, K.L. Giboni, S. Kamat, P. Majewski, K. Ni, B.K. Singh and M. Yamashita., "Performance of Dual Phase Xe-TPC with CsI Photocathode and PMTs readout for the Scintillation Light," *IEEE ICDL,* p. 345, 2005.

[34] S. E. Derenzo et al. , "Electron Avalanche in liquid xenon," *Phys. Rev. A,* vol. 9, pp. 2582-2591, 1974.

[35] M. Miyajima et al., "Proportional counter filled with highly purified liquid xenon," *Nucl. Instrum. Meth,* vol. 160, pp. 403-405, 1979.

[36] E. Aprile, H. Contreras, L.W. Goetzke, A.J. Melgarejo Fernandez, M. Messina, J. Naganoma, G. Plante, A. Rizzo, P. Shagin, R. Wall, "Measurements of proportional scintillation and electron multiplication in liquid xenon using thin wires," *JINST,* vol. 9 P11012, 2014.

[37] T. Ye, K.L. Giboni and X. Ji, "Initial evaluation of proportional scintillation in liquid Xenon for direct dark matter detection," *JINST,* vol. 9 P12007, 2014.

[38] A. Buzulutskov, "Advances in Cryogenic Avalanche Detectors," *JINST 7 C02025,* 2012.

[39] P. K. Lightfoot, G. J. Barker, K. Mavrokoridis, Y. A. Ramachers, and N. J. C. Spooner, "Optical readout tracking detector concept using secondary scintillation from liquid argon generated by a thick gas electron multiplier," *JINST 4 P04002,* 2009.

[40] F.D. Amaro, J.M.F. dos Santos, J.F.C.A. Veloso, A. Breskin, R. Chechik, A. Lyashenko, "The photonassisted cascaded electron multiplier operation in CF4 for ion backflow suppression," *IEEE Trans. Nucl. Sci.,* vol. 55, pp. 1652-1656, 2008.

[41] A Buzulutskov and A Bondar, "Electric and Photoelectric Gates for ion backflow suppression in multi-GEM structures," *JINST,* 2006 1 P08006.

[42] L. Arazi, A. Breskin, A. Coimbra, T. Itay, H. Landsman, M. Rapaport, D. Vartsky, "First observation of electrolumineschence in liquid xenon within THGEM holes," *JINST,* vol. 8 C12004, 2013.

[43] T. Doke, "Recent developments of liquid xenon detectors," *Nucl. Instrum. Meth,* vol. 196, pp. 87-96, 1982.

[44] National Nuclear Data Center, "Decay Radiation of Am241," [Online]. Available: http://www.nndc.bnl.gov/chart/decaysearchdirect.jsp?nuc=241AM&unc=nds. [Accessed 2015].

[45] L. Arazi, A. E. C Coimbra, I. Israelashvili, E. Erdal, M. L. Rappaport, D. Vartsky and A. Breskin, "Gaseous photomultipliers and liquid hole multipliers for future noble-liquid detectors," in *7th symposium on Large TPCs for Low-Energy Rare-Events detection*, Paris, 2014.

[46] L. Arazi, E. Erdal, A. E. C. Coimbra, M. L. Rappaport, D. Vartsky, V. Chepel and A. Breskin, "Electroluminescence in THGEM liquid hole- multipliers through gas bubbles in liquid xenon," *in preparation.*

[47] M. Hribar, A. Kodre and J. Pahor, "The determination of the K-shell fluorescence yield of xenon by use of the proportional counter method," *Z. Physik A,* vol. 280, pp. 227-229, 1977.

[48] Werner F. Schmidt, Liquid State Electronics of Insulating Liquids, Boca Raton, Florida: CRC Press LLC, 1997.

[49] B.A. Dolgoshein, A.A. Kruglov, V.N. Lebedenko, V.P. Miroshnichenko, B.U. Rodionov, "Electronic method of particle detection in double phase liquid-gas systems," *Physics of Elementary Particles and Atomic Nucleus,* vol. 4, no. 1, pp. 167-186, 1973.

[50] H.L. Brooks et al., "Electron drift velocities in xenon," *J. Phys. D: Appl. Phys.,* vol. 15, no. 6, 1982.

[51] E. Aprile, R. Mukherjee, M. Suzuki, "Ionization of liquid xenon by 241Am and 210Po alpha particles," *Nucl. Intrum. and Meth.,* vol. 307, no. 1, p. 119–125, 1991.

[52] G. Bressi, M. Cambiaghi, G. Carugno, E. Conti, and E. D'Uscio, "Electron multiplication in liquid argon on a tip array," *Nucl. Instrum. Meth. A 310,* p. 613–617, 1991.

[53] L. Subtil et al., "VUV Optical Constants of Liquid and Solid Xenon at the Triple Point," *physica status solidi (b),* vol. 143, no. 2, p. 783–793, 1987.

[54] L. M. Barkov et al., "Measurement of the refractive index of liquid xenon for intrinsic scintillation light," *Nucl. Instum. and Meth.,* vol. 379, no. 3, pp. 482-483, 1669.

[55] V. N. Solovov et al., "Measurement of the refractive index and attenuation length of liquid xenon for its scintillation light," *Nucl. Instum. and Meth.,* vol. 516, no. 2-3, pp. 462-474, 2004.

[56] NIST, "Thermophysical Properties of Fluid Systems," [Online]. Available: http://webbook.nist.gov/chemistry/fluid/. [Accessed 2015].

[57] Planck Collaboration: P. A. R. Ade et al., "Planck 2013 results. XVI. Cosmological parameters," *Astronomy and Astophysics,* vol. 571 A16, 2014.

[58] C M B Monteiro et al, "Secondary scintillation yield in pure xenon," *JINST,* vol. 2 P05001, 2007.

[59] K. MASUDA et al., "A liquid xenon proportional scintillation counter," *Nucl. Instum. and Meth.,* vol. 160, pp. 247-253, 1979.